Examining the chemistry of atmospheric mercury using aircraft-based measurements and a global chemical transport model

Viral Pinakin Shah

A dissertation

submitted in partial fulfillment of the

requirements for the degree of

Master of Science

University of Washington

2015

Reading Committee:

Lyatt Jaeglé, Chair

Dan Jaffe

Becky Alexander

Program Authorized to Offer Degree:

Department of Atmospheric Sciences

University of Washington

Abstract

Examining the chemistry of atmospheric mercury using aircraft-based measurements and a global chemical transport model

Viral Pinakin Shah

Chair of the Supervisory Committee:
Professor Lyatt Jaeglé
Department of Atmospheric Science

Mercury is a potent neurotoxin that accumulates in fish and enters the human food chain. The largest source of mercury to the oceans is from the deposition of atmospheric mercury. Oxidized mercury species (Hg(II)) in the atmosphere are highly soluble and deposit efficiently; thus strongly influence the amount and the spatial distribution of mercury deposition. Currently, the distribution of oxidized mercury species in the atmosphere, and their source from *in situ* oxidation of elemental mercury (Hg(0)) by reaction with bromine atoms remain poorly understood. The Nitrogen, Oxidants, Mercury, and Aerosol Distribution, Sources, and Sinks (NOMADSS) aircraft experiment was designed with the aim of addressing these limitations. Speciated mercury concentrations were measured over the Southeastern US between June 1 and July 15, 2013 using a novel instrument developed at the University of Washington-Bothell. In this thesis, I use the GEOS-Chem chemical transport model to interpret the NOMADSS mercury measurements, and place new constraints on mercury chemistry in the free troposphere.

The mean (and standard deviation) of the observed concentration of total atmospheric mercury (THg) was 1.49 ± 0.16 ng/m^3, while that of Hg(II) was 111 ± 106 pg/m^3. 60% of the

Hg(II) observations were below the instrument's limit of detection. High concentrations of Hg(II) (300-680 pg/m^3) were observed in clean, dry air masses originating in the upper troposphere of the subtropical anticyclones, where fast production and lack of deposition lead to accumulation of Hg(II). The mean THg concentrations modeled by GEOS-Chem are found to be in close agreement with the observations. In contrast, the modeled Hg(II) concentrations are found to be low by a factor of three relative to the observations, indicating a faster than expected oxidation rate.

I perform two sensitivity simulations with GEOS-Chem: (i) by increasing bromine radical concentrations by a factor of three, and (ii) by using a faster oxidation rate constant. The model underestimate of observed Hg(II) concentrations in the clean, dry air masses is reduced from a factor of 3 to factors of 2 and 1.6 in the two sensitivity simulations. The modeled lifetime of Hg(0) against oxidation to Hg(II) decreases from 4.8 months in the base simulation to 2.8 months and 1 month, respectively, in the sensitivity simulations. The model predicts that the 500 hPa summertime Hg(II) concentrations are three to five times higher in the subtropical anticyclones than elsewhere, highlighting the role of these regions as significant reservoirs for the global long-range transport of Hg(II). The model results imply that the faster oxidation of Hg(0) leads to a significant increase in the importance of reduction of Hg(II) in the cycling of mercury in the atmosphere.

TABLE OF CONTENTS

LIST OF FIGURES

LIST OF TABLES

ACKNOWLEDGEMENTS

I thank the National Science Foundation for funding this work (award # ATM-1217010). I thank Jesse Ambrose, Lynne Gratz, and Dan Jaffe for sharing their mercury observations with me and for the helpful discussions during my analysis of the observations. I thank all NOMADSS participants for making their observations available for use. I am grateful to Dan Jaffe and Becky Alexander for serving on my reading committee and for their recommendations for making my thesis stronger. I am immensely grateful to Lyatt Jaeglé for her unwavering support through the course of this thesis, and for nurturing me in the early stages of my research career.

Chapter 1. INTRODUCTION

Mercury poses severe risks to human and ecosystem health. It is a potent toxin that targets the human nervous system, hinders the cognitive development of children, and causes cardiovascular diseases in adults (*Mergler et al., 2007; Karagas et al., 2012*). In fish, mammals, and birds, exposure to mercury can adversely affect reproductive behavior (*Scheuhammer et al., 2007*). The primary route of mercury exposure in humans and wildlife is through consumption of food contaminated with methylmercury. Methylmercury is not only efficiently taken up by microbes at the bottom of the food chain, but, more importantly, it bioaccumulates and magnifies at higher trophic levels (*Morel et al., 1998*). Piscivorous fish, such as tuna and swordfish, can thus contain mercury concentrations that are 6-7 orders of magnitude higher than their environment (*Fitzgerald et al., 2007*). Recent evidence has revealed that methylmercury can accumulate in rice crop, as well (*Li et al., 2010*). Although mercury is naturally present in trace amounts in our environment, human activities have increased its levels by factors of 3 to 7 (*Lamborg et al., 2002; Selin, 2009*; *Amos et al., 2013, Zhang et al., 2014*) making it a major public health concern.

Mercury exists in the Earth's crust primarily as HgS (cinnabar ore). In the atmosphere, mercury is present as a gaseous element (Hg(0)), or in the oxidized (mercuric, +2) state (Hg(II)). Atmospheric Hg(II) can exist either in the gas-phase or bound to particles. The chemical forms of atmospheric Hg(II) have not been identified, but laboratory studies suggest that possible forms include $HgCl_2$, $HgBr_2$, HgO, $HgSO_4$, $Hg(NO_2)_2$, $Hg(OH)_2$ (*Gustin et al., 2013*). In the ocean waters and lakes, mercury is found in the dissolved elemental form, a variety of inorganic oxidized forms, and organic forms that include methylmercury (*Fitzgerald et al., 2007*). Mercury cycles between the Earth's surface reservoirs and the lithosphere on timescales of thousands of years (*Mason and Sheu, 2002; Selin et al., 2008*). Mercury is mobilized form from the Earth's crust through natural processes of volcanism, and through human activities such as mining and burning of fossil fuels. Both natural and human processes emit mercury largely to the atmosphere. In the atmosphere, mercury is transported and eventually deposited to the land and ocean surfaces. A small fraction of the deposited mercury is converted to methylmercury by anaerobic bacteria, and is subsequently absorbed in the food chain. However, most of the deposited mercury is not methylated, but is re-volatilized as Hg(0) to the atmosphere. Thus emissions of mercury can be classified as primary (initial mobilization from the lithosphere through volcanism or anthropogenic activities) and secondary (reemission of previously deposited mercury). Current primary emissions from human activities are estimated at 2300 Mg/a, compared to primary natural emissions of 90 Mg/a (1Mg/a=10^6 g per year), whereas secondary emissions from the land and ocean are estimated at 5100 Mg/a (*Pirrone et al, 2010*).

In the atmosphere, mercury is present at a background concentration of 1.5-1.7 ng/m^3 in the Northern Hemisphere, and at 1.1-1.3 ng/m^3 in the Southern Hemisphere (*Lindberg et al., 2007*) (1 m^3, here, represents 1 standard-m^3, that is 1 m^3 of dry air at 273.15 K and 1 atm, thus 1 ng/m^3 = 0.112 pptv). Mercury concentrations are almost uniform at the surface throughout each hemisphere and across the depth of the troposphere. The inter-hemispheric gradient and the uniformity of mercury distribution indicate a long residence time of mercury in the atmosphere. The residence time is estimated to be between six months and a year (*Driscoll et al., 2013*). While in the atmosphere, mercury can be transported to remote regions of the planet, making mercury not only a local, but also a global pollutant.

Natural and most of the anthropogenic processes emit mercury to the atmosphere as Hg(0). Hg(II) compounds are emitted in smaller quantities mainly from combustion processes. In the global troposphere, about 90% of the mass of total mercury (THg, THg ≡ Hg(0)+Hg(II)) is in the form of Hg(0) (*Selin et al, 2008; Holmes et al., 2010*). Hg(II) originates predominantly from the oxidation of Hg(0). Compared to Hg(0), Hg(II) is highly water-soluble and reactive, and is quickly scavenged from the atmosphere by rainwater and aerosol particles. The residence time of Hg(II) in the atmosphere is on the order of days to weeks. Since Hg(II) deposits readily, despite its presence in smaller amounts relative to Hg(0), it makes a larger contribution to the global deposition flux of mercury. About 60% of the global mercury deposition occurs by wet and dry deposition of Hg(II). Thus speciated mercury measurements (simultaneous measurements of Hg(0) and Hg(II)) in the atmosphere are essential in understanding the fate of mercury in the environment.

Speciated mercury measurements are continuously made at dozens of surface-based sites in the northern hemisphere as part of the European Monitoring and Evaluation Programme (www.emp.int), Canadian Atmospheric Mercury Measurement Network (http://www.msc.ec.gc.ca/arqp/camnet_e.cfm), Atmospheric Mercury Network in USA (http://nadp.sws.uiuc.edu/amn/), and the Global Mercury Observation System (www.gmos.eu). Intensive measurement campaigns have focused on specific environments, such as the marine and polar boundary layers (see *Sprovieri et al, 2010b* for a comprehensive review). These measurements suggest that Hg(II) concentrations at the surface are generally below 50 pg/m^3 (1 pg/m^3 = 10^{-3} ng/m^3). Hg(II) concentrations of ~1000 pg/m^3 can be present in areas downwind of emission sources (*Poissant et al., 2005*), or during Mercury Depletion Events, when Hg(II) is formed from rapid oxidation of Hg(0) (*Cobbett et al., 2007*). Very few studies have quantified Hg(II) levels in the free troposphere. Measurements at the few high-elevation monitoring sites have shown the presence of large amounts of Hg(II) in the free troposphere. Landis et al. (*2005*) measured ~350 pg/m^3 of Hg(II) at Mauna Loa, Hawaii (3397 m above sea level), whereas Swartzendruber et al. (*2006*) measured up to 600 pg/m^3 of Hg(II) at the Mt. Bachelor Observatory in Oregon (2731 m asl). At these and other sites (*Fain et al., 2009, Sheu et al., 2010, Weiss-Penzias et al., 2015*) elevated Hg(II) concentrations were seen in low relative humidity and low CO air, suggesting that the origin of the Hg(II) is from atmospheric oxidation in the free troposphere and not from local pollution sources.

Measurements of the vertical distribution of both THg and Hg(II) from an aircraft platform have been made only in the past 10 years. The earliest aircraft measurement of Hg(II) were made by Sillman et al., (*2007*) off the coast of Florida. They reported that Hg(II) concentrations were higher (10-248 pg/m^3) in the free troposphere than in the boundary layer (<40 pg/m^3), and the enhancements were seen in air with a cloud-free history. However, their instrument had a low time resolution. A single denuder was used to collect Hg(II) sample for each flight, and thus the Hg(II) concentrations reported were the average concentrations for the entire flight. The University of Washington Detector of Oxidized Hg Species (UW-DOHGS) developed by Professor Dan Jaffe's research group is the only instrument that can measure speciated mercury concentrations aboard an aircraft platform at a high time resolution of 2.5 minutes. Swartzendruber et al. (*2009*) made the first measurements using this instrument during five flights over the Pacific Northwest. They reported large variability in the Hg(II) concentrations (0-500 pg/m^3) in the bottom 5 km of the troposphere. They found enhanced Hg(II) concentrations in the free troposphere in air with low aerosol scattering coefficient. Using this instrument, Lyman and Jaffe (*2012*), found enhanced Hg(II) concentrations of ~450 pg/m^3

and depleted THg concentrations (<1 ng/m^3) in a stratospheric intrusion, suggesting rapid oxidation and loss of THg above the tropopause.

However, these aircraft-based measurements have been limited to small spatial scales. Determining the distribution of THg and Hg(II) at the regional scale is important in understanding the processes governing the cycling of mercury in the global troposphere. This led to the Nitrogen, Oxidants, Mercury and Aerosols Distributions, Sources, and Sinks (NOMADSS) experiment. The UW-DOHGS, along with several other instruments, was deployed on NSF/NCAR's C130 aircraft from 1 June to 15 July, 2013 to measure the distribution of mercury over the southeast US. Here, I present an analysis of these first large-scale speciated measurements of mercury in the free troposphere.

Several global chemical transport models have been developed to study the fate of mercury in the atmosphere (for example, *Bergan et al., 1999; Seigneur et al., 2001; Dastoor and Larocque, 200; Jaeglé et al., 2009; Jung et al., 2009*). These models have been used to understand the spatial and seasonal patterns of mercury deposition, inter-hemispheric gradient in mercury concentrations, trends in mercury concentration and deposition, intercontinental transport of mercury, and source-receptor relationships. However, the physical and chemical processes controlling the fate of mercury in the atmosphere are complex and poorly understood. As a result, different models make different simplifying assumptions to simulate these processes, which leads to a large spread in the model results. To test the influence of these simplifications, an inter-comparison study of three regional models for North America was conducted (*Bullock et al., 2008; Bullock et al., 2009*). Despite the use of identical emissions, meteorology, initial/boundary conditions, and spatial resolution, the simulated mean wet deposition over the domain varied by 70% among the models. At certain locations, the spread in the dry deposition flux was up to a factor of ten high. In a different inter-comparison study of five global/hemispheric models, all models were found to simulate the concentrations of Hg(0) within 15-20% of each other, but the wet deposition in most regions varied by a factor ~2 and the dry deposition varied by a factor of ~5-7 (*Travnikov et al., 2010*). Since Hg(II) concentrations strongly influence the wet and dry deposition fluxes, the inter-model differences in simulating these quantities reflect the uncertainties in emissions and production of Hg(II) and the lack of speciated free tropospheric Hg(II) measurements to validate these models.

The redox chemistry of atmospheric mercury is one of the most uncertain processes. Laboratory studies suggest that the gas-phase oxidation of Hg(0) can occur by reaction with common atmospheric oxidants: O_3 (*Hall, 1995; Spicer et al., 2002; Pal and Ariya, 2004a; Sumner et al., 2005; Rutter et al., 2012*), OH (*Sommar et al., 2001; Pal and Ariya, 2004b*), Br (*Ariya et al., 2002; Donohoue et al., 2006*), Br_2 (*Ariya et al, 2002*), BrO (*Spicer et al., 2002; Raofie and Ariya, 2004*), Cl (*Ariya et al., 2002; Donohoue et al., 2005; Byun et al., 2010*), Cl_2 (*Ariya et al., 2002*), IO (*Raofie et al., 2008*), I (*Raofie et al., 2008*), I_2 (*Raofie et al., 2008*), and NO_3 (*Sommar et al., 1997; Spicer et al., 2002; Sumner et al., 2005*). However, chemical composition of atmospheric Hg(II) remains unknown. Current instruments that can detect Hg(II) *in situ* are capable of measuring its concentration (by collecting it on denuders or filters), but can not differentiate between specific forms of Hg(II). This makes it difficult to determine the importance of these oxidants of Hg(0) in the atmosphere (*Gustin and Jaffe, 2010; Jaffe et al, 2014*). Our current understanding of the dominant mechanism of atmospheric oxidation of Hg(0) is based on laboratory studies, theoretical calculations, and indirect evidence from simultaneous measurements of mercury and other relevant species.

The Br radical is widely accepted as the dominant oxidant of Hg(0) in the global atmosphere. Field-evidence for fast Br-induced oxidation comes from studies mainly in the polar and the marine boundary layers (*Lindberg et al., 2002; Ebinghaus et al., 2002; Laurier et al, 2003; Obrist et al., 2011*). Laboratory and theoretical studies have elucidated the reaction mechanism and have demonstrated the atmospheric viability of this oxidation pathway (*Ariya et al., 2002; Donohoue et al., 2006; Goodsite et al., 2012; Dibble et al., 2012; Shepler et al., 2007*). However, the spread among the reaction rates calculated in these studies is a factor of ten. Furthermore, this oxidation mechanism and its kinetics in the free troposphere remain largely untested.

The oxidation of Hg(0) by O_3 and OH has also been proposed as a viable pathway, but it has not been accepted by many. Studies by Calvert and Lindberg (*2005*), Goodiste et al. (*2004*), and Hynes et al. (*2009*), on the one hand, suggest that the bimolecular reaction of Hg(0) with O_3 and OH may be too slow in the atmosphere, but laboratory-based studies, on the other hand, have consistently reported rates that are ~100 times faster (*Pal and Ariya, 2004a; Sumner et al., 2005, Rutter et al., 2012*). It is not clear whether the fast reaction seen in the laboratory studies is due to secondary wall-mediated reactions, or from a more complex mechanism involving the formation of aerosol particles as products of the oxidation pathway (*Tossell, 2006*). Nevertheless, many of the current chemical transport models use only the Hg(0)+O_3 and Hg(0)+OH oxidation mechanism, mainly because of uncertainties in the distribution of Br in the atmosphere (*Subir et al., 2011*).

GEOS-Chem is one of the few chemical transport models that use the Br oxidation pathway, and has been evaluated extensively with surface-based measurements of ambient speciated concentrations and wet deposition fluxes, and, to a lesser extent, with aircraft-based measurements of Hg(0) (*Holmes et al., 2010; Amos et al., 2011; Zhang et al., 2012*). In this study, I use the GEOS-Chem model to test the kinetics of the Br-induced oxidation mechanism by comparing the model results with the NOMADSS observations. The NOMADSS observations present the first opportunity to thoroughly test the GEOS-Chem model's predictions of mercury speciation in the free troposphere.

In Chapter 2, I describe the NOMADSS experiment, the UW-DOHGS instrument, and the GEOS-Chem model. I also discuss in detail the uncertainty in the oxidation chemistry of Hg(0), and the sensitivity simulations I perform with the model to test the effects of these uncertainties. In Chapter 3, I present the observed distribution of mercury over the Southeast US and compare it to the model results. The key finding is that the observations suggest a very fast oxidation rate of Hg(0) in the free troposphere. I end with a brief discussion on the potential implications of this faster oxidation on the global distribution and budget of atmospheric mercury.

Chapter 2. OBSERVATIONS AND MODEL SIMULATIONS

2.1 THE NOMADSS EXPERIMENT

The NOMADSS aircraft experiment was performed over the Southeastern US from June 1 to July 15, 2013. The NSF/NCAR C-130 aircraft was stationed in Smyrna, TN (36°N, 86.5°W), from where 19 research flights of 4-7 hours duration were conducted (Figure 2.1). The C-130 can reach an altitude of about 8 km, and has a 2800 km range when flying in the lower troposphere. NOMADSS is part of the Southeast Atmosphere Study (SAS), a large collaborative effort to characterize the atmospheric composition over the southeast US (http://www.eol.ucar.edu/field_projects/sas). One of the objectives of the NOMADSS experiment is to quantify the tropospheric distribution of mercury species in the region.

The aircraft was equipped with several instruments to measure the concentrations of mercury species, oxidants, including OH, HO_2, O_3, and BrO, combustion products such as CO, NO_x and SO_2, inorganic nitrogen compounds, several VOCs, particle size distributions and number concentration, and common meteorological parameters. Table 2.1 has a list of the species that I have used in this study.

Table 2.1. Chemical and meteorological measurements used in this work.

Observations	Measurement technique	Instrument model / Reference
THg, Hg(0), Hg(II)	Dual-channel CVAFS (UW-DOHGS)	Lyman and Jaffe (*2011*); Ambrose et al. (*2013; 2015*)
RH	Chilled mirror hygrometer	Buck 1011C
CO	Vacuum-UV Resonance Fluorescence	Aero-Laser AL5001
NO, NO_2, O_3	NO_2 chemiluminescence	Ridley et al. (*2004*)
CH_2O, $CHBr_3$, CH_2Br_2, DMS	Gas chromatograph/ Mass spectrometer	Apel et al. (*2010*)
BrO	Differential Optical Absorption Spectroscopy	Platt and Stutz (*2008*)

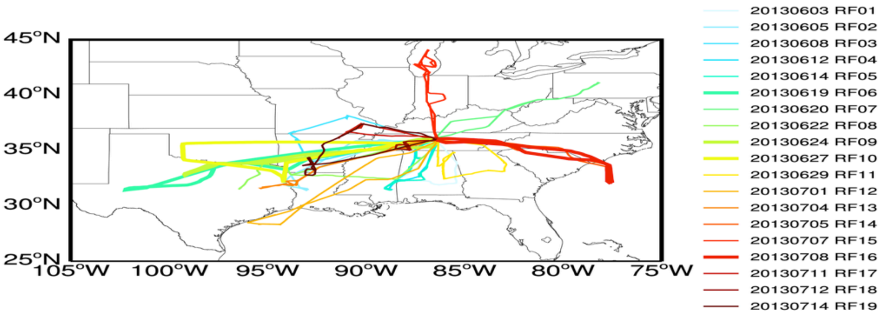

Figure 2.1. Flight tracks of the 19 NOMADSS research flights between June 1 and July 15, 2013.

2.2 THE UW-DOHGS INSTRUMENT

The UW-DOHGS measures THg and Hg(0) simultaneously at a time resolution of 2.5 minutes. Ambient air samples are collected from a rear-facing aircraft inlet heated to 110°C. Two Tekran® 2537B Cold Vapor Atomic Fluorescence Spectrometers (CVAFS) subsample from the ambient air at 1 standard liter per minute. The sample line of the first CVAFS is packed with heated (650°C) quartz wool to convert all oxidized mercury species to the elemental form. Thus the concentration measured by the first CVAFS corresponds to that of THg present in the sampled air. The sample line of the second CVAFS contains an Hg(II) filter, and this CVAFS measures the concentrations of Hg(0) in the sampled air. A quartz wool trap was used as the Hg(II) filter during the first thirteen flights, and a cation exchange membrane for the remaining six flights.

Hg(II) concentrations are calculated from the difference between the measurements of the two CVAFS's, after adjusting for any bias between them. The bias is determined using a 'same-air' configuration, during which the Hg(II) filter is bypassed and both the channels measure THg concentrations from the same air stream. Tests conducted during RAMIX (*Ambrose et al., 2013*) and in the laboratory show that the UW-DOHGS responds linearly to spikes in $HgBr_2$ (a surrogate Hg(II) compound), and has an Hg(II) recovery of 66%. The instrument is not prone to O_3-interference, unlike the Tekran speciation system, which uses KCl denuders as the Hg(II) filters (*Lyman et al., 2010; McClure et al., 2014*). One issue is that the retention efficiency of the Hg(II) filters used by the UW-DOHGS, especially quartz wool, is low in humid conditions. This significantly limits the instrument's ability to measure Hg(0) (and Hg(II)) under typical boundary layer conditions.

The uncertainty in the THg and Hg(0) measurements arises mainly from the uncertainty of the CVAFS response factors (peak fluorescence intensity per unit mass of Hg), and in measuring the flow rate through the CVAFS. The 1-sigma uncertainty in THg and Hg(0) for the NOMADSS flights was between 8 and 10%. The uncertainty in Hg(II) measurements depends on the uncertainty in measuring the bias between the two CVAFS, which is a function of the THg concentrations. The 1-sigma uncertainty varies between 38 and 55 pg/m^3. The limit of detection (LOD) for Hg(II) is estimated by periodically configuring the instrument to run in the 'same-air' configuration. The 3-sigma LOD ranged between 57 and 228 pg/m^3. Ambrose et al. (*2015*) present further details of the UW-DOHGS instrument, including its configuration, in-flight calibration procedures, and pre- and post-campaign laboratory tests.

2.3 THE GEOS-CHEM MODEL

GEOS-Chem is a state-of-the-art three-dimensional atmospheric chemical transport model that is developed, used, and maintained by a vast community of researchers across the world. It relies on NASA GMAO's GEOS modeling system for the pertinent meteorological fields. The GEOS system consists of a general circulation model coupled with a data assimilation system (*Reinecker et al., 2008*). The model has a horizontal resolution of 0.25° latitude ×0.3125° longitude with 72 vertical levels up to 0.01 hPa. The model output is archived either at 1-hour or 3-hour intervals. GEOS-Chem includes advection (*Lin and Rood, 1996*), convective transport (*Wu et al., 2007*), turbulent mixing (*Lin and McElroy; 2010*)), wet deposition (*Liu et al., 2001; Wang et al., 2011; Amos et al., 2012*), and dry deposition (*Wang et al., 1998; L. Zhang et al., 2011*) of chemical species. The full-chemistry simulation includes an up-to-date chemical mechanism for gas-phase and heterogeneous reactions of HOx-NO_x-VOC-O_3-BrO_x in the troposphere (*Bey et al., 2001; Parella et al., 2012*). The mercury simulation is performed in a standalone manner, but depends on the results of the full-chemistry simulation for concentrations of oxidants and aerosol particles.

In this study, the model is run in a one-way nested-grid configuration, with the native horizontal resolution (0.25° latitude ×0.3125° longitude) over North America, and a coarser resolution (4° latitude×5° longitude) over the rest of the globe. Both, the coarse- and fine-grid models, have 47 layers in the vertical, with 13 layers in the bottom 2 km, and 16 layers between 2 and 10 km. I first run the 4°×5° global full-chemistry model to generate the boundary conditions for the nested-domain, and to archive the oxidant concentrations for the mercury simulation. I run the 0.25°×0.3125° full-chemistry model for North America from June 1 to July 15, 2013. For comparison to the NOMADSS aircraft observations, the full-chemistry model is sampled at 1-minute interval along the flight tracks.

2.3.1 *Results of the full-chemistry simulation*

Figure 2.2 shows a comparison of the results of the GEOS-Chem full-chemistry nested-grid simulation with the NOMADSS observations of RH, CO, NO_x, O_3, CH_2O, and BrO. The model generally reproduces the observed mean values for these species. The model captures very well the mean RH (model mean ± standard deviation: 49 ± 25%, observed: 50 ± 26%) reflecting a good overall representation of the meteorological conditions during NOMADSS (Figure 2.2A). The model displays a similar level of agreement for temperature (model: 283±12 K, observations: 283±16 K) and winds (model: 'u' 4.9 ± 3.9 m/s, 'v' 3.9 ± 4.0 m/s, observations: 'u' 5.6 ± 3.9 m/s, 'v' 4.2 ± 3.8 m/s), as well.

For CO, the model has a 10-15 ppbv negative bias relative to the observations (Figure 2.2B). The observed and simulated NO_x agree well in the lower troposphere, but above ~5km altitude, the model is significantly too high, possibly reflecting an overestimate in lightning NOx (Figure 2.2C). The similarity between the model and observations for O_3 (model: 63±11 ppbv; observations: 56±14 ppbv) and CH_2O (model: 1.31±1.28 ppbv, observations: 1.71±1.25 ppbv) (Figures 2.2D and 2.2E), in addition to that of CO and NO_x, shows that the model does well in simulating the complex chemical and physical processes that govern the concentrations of these tropospheric chemical species. For BrO (Figure 2.2F), however, the model is low by a factor of five compared to the one observation made during flight RF-06 over Texas (*Gratz et al., 2015*).

In a previous comparison of the GEOS-Chem full-chemistry simulation with aircraft-based observations over central and eastern US (NASA Intercontinental Transport Experiment-North America (INTEX-NA)), the modeled CO, NO_x, CH_2O and O_3, were found unbiased relative to the observations between 2 and 6 km altitudes (*Hudman et al., 2007*). Below 2 km, the modeled CO and NO_x were about 20% higher than the observations.

2.4 THE GEOS-CHEM HG MODEL

The GEOS-Chem mercury model simulates the emissions, chemistry, transport, and deposition of Hg(0) and Hg(II) in the atmosphere. The gas and particle phases of Hg(II) are treated separately. The model was initially developed by Selin et al. (*2007*), Selin et al. (*2008*), and Strode et al. (*2007*), and updated by Soerensen et al. (*2010*), Holmes et al. (*2010*), Zhang et al. (*2012*), and Amos et al. (*2012*). The ocean is represented as a 2-D surface, where reduction and oxidation processes between the mercury species, and their exchange with the atmosphere and the deep ocean is simulated (*Strode et al., 2007; Soerensen et al., 2010*). The land, too, is treated as a 2-D slab, which receives deposition flux from the atmosphere, rapidly re-emits part of the deposited mercury, and transfers the rest to longer-lived land reservoir (*Selin et al., 2008; Holmes et al., 2010*). Mercury from the land reservoir gradually evades to the atmosphere in the presence sunlight, and during evapotranspiration. Mercury deposited to snow surfaces is re-emitted to the atmosphere in 1 week when temperatures are below -3°C and in six months at warmer temperatures. The model includes emissions from biomass burning and geogenic activity (*Holmes et al., 2010*). The mercury emitted to the atmosphere from the above processes is in the form of Hg(0).

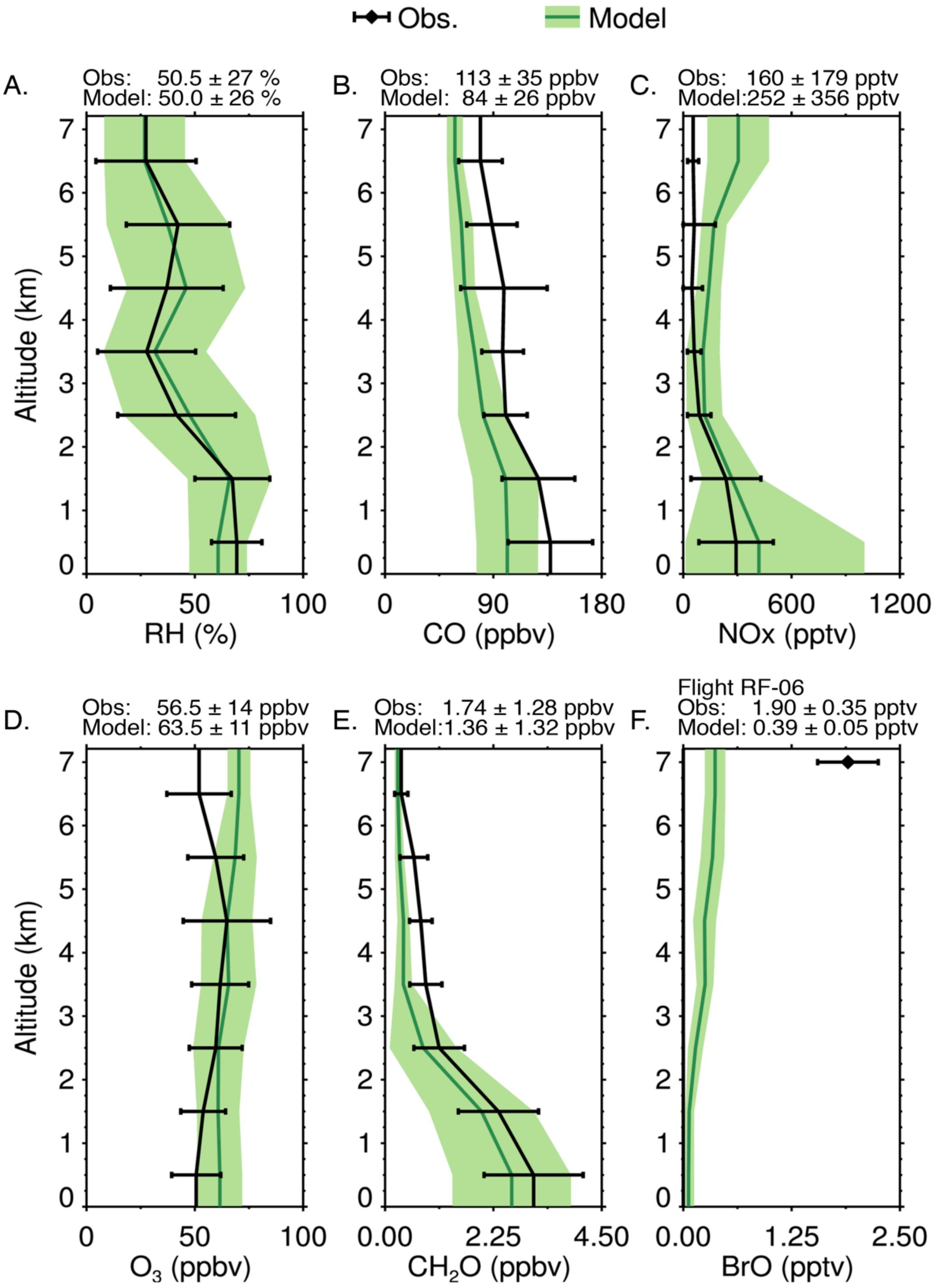

Figure 2.2. A comparison of the vertical profiles of the observed and simulated values of RH (A), CO (B), NOx (C), O_3 (D), CH_2O (E), and BrO (F). The means and standard deviations calculated for 1 km high vertical bins are shown (observations: black error bars, model: green line and shading).

Global anthropogenic emissions of mercury were previously based on the GEIA 2005 inventory (*Pacyna et al., 2010*), and on the US EPA's National Emissions Inventory (NEI) 2005 (http://www.epa.gov/ttnchie1/net/2005inventory.html) and Environment Canada's National Pollutant Release Inventory (NPRI) 2005 (https://www.ec.gc.ca/inrp-npri/) inventories for North America. In this study I have updated the anthropogenic emissions to the more recent UNEP/AMAP 2010 (http://www.amap.no/mercury-emissions/datasets), and the NEI 2011 (http://www.epa.gov/ttnchie1/net/2011inventory.html) and NPRI 2011 emission inventories. The speciation of anthropogenic emissions is assumed to be 90% (Hg(0)): 10% (Hg(II)) from all sources following the findings of Kos et al. (*2013*). This is a little different from the speciation of 86.5 %(Hg(0)): 13.5% Hg(II) for emissions from power plants and waste incinerators considered by Zhang et al. (*2012*). The annual global emission of mercury from anthropogenic sources is 1900 Mg/a, and from natural sources is about 5000 Mg/a. Over North America, the anthropogenic and natural emissions are 65 Mg/a and 475 Mg/a respectively.

The oxidation of Hg(0) is simulated to occur by reaction with bromine atoms (Br). Br concentrations at each time step are calculated by imposing a diurnal cycle on the monthly-averaged concentrations archived from the full-chemistry simulation. The simulated oxidation mechanism is discussed in further detail in Section 2.4.1. The reduction of Hg(II) to Hg(0) is assumed to occur in cloud droplets in the presence of sunlight. We assume that the reduction is proportional to the photolysis frequency of NO_2 and the coefficient is estimated by constraining the model results with the observed mean burden of THg in the troposphere.

The gas-particle partitioning of Hg(II) follows two separate pathways. In the moist marine boundary layer, gas-phase Hg(II) dissolves in deliquesced sea-salt particles, and instantly deposits to the ocean surface. The uptake of Hg(II) by sea-salt particles is simulated as a kinetic mass transfer process as described in Holmes et al. (*2009*) and Holmes et al. (*2010*). The second pathway follows the surface adsorption of gas-phase Hg(II) onto non sea-salt aerosol particles. This is simulated as an equilibrium partitioning process based on an empirical temperature-dependent coefficient (*Amos et al., 2012*). Both the gas- and particle-phases of Hg(II) participate equally in the chemical reactions. However, they undergo deposition processes that are characteristic of their respective states. The wet and dry deposition of gas-phase Hg(II) is analogous to that of HNO_3, and the wet and dry deposition of particle-bound Hg(II) is analogous to that of sulfate particles.

In a previous evaluation of the global GEOS-Chem model, Holmes et al. (*2010*) compared the model results to 39 land-based sites across the globe, and found the model THg (1.71 ± 0.5 ng/m^3) to be in good agreement with observations (1.86 ± 1.0 ng/m^3, r^2=0.81). The model reproduced the observed minimum in THg concentrations during late summer at 15 sites in the northern mid-latitudes, and the depletion of mercury during early spring at the Arctic sites (*Holmes et al., 2010*). The simulated THg concentrations were ~10% higher than the THg concentrations measured during three aircraft campaigns (INTEX-B, CARIBIC, and ARCTAS), but the modeled vertical profiles were consistent with the observations in the troposphere (*Holmes et al., 2010*).

Zhang et al. (*2012*) evaluated the 0.5°×0.667° nested-grid model with surface-based observations over North America. They found that the average annual modeled wet deposition (7.2 ± 3.2 μg/m^2-yr) at 95 Mercury Deposition Network (MDN) sites was close to the observations (8.8 ± 3.6 μg/m^2-yr) and showed a correlation coefficient of 0.78. The modeled annual mean THg concentrations (1.42 ± 0.11 ng/m^3) were unbiased with respect to the observations (1.46 ± 0.11 ng/m^3) at 19 surface-based sites. While the modeled gaseous Hg(II) concentrations at these sites were higher than the observations by a factor of ~1.5, the model captures the seasonal cycle of higher concentrations during spring and summer at most sites.

I have developed a new 'tagged' Hg(II) simulation to identify the regions where Hg(II) is chemically produced. I divide the global domain into seven regions, and track the Hg(II) produced in each of these regions as separate model tracers which undergo all of the physical and chemical processes described above. In the vertical, the domain is divided into four regions (Figure 2.3B): boundary layer (BL), middle troposphere (MT, defined as the region between the top of the boundary layer and 350 hPa), upper troposphere (UT, defined as the region between 350 hPa and the tropopause), and the stratosphere (ST, region from the tropopause to 0.01 hPa). The upper tropospheric (UT) region is further divided into four sub-regions (Figure 2.3A): Pacific Ocean (PA), North America (NA), the rest of the northern hemisphere (NH), and the southern hemisphere (SH). Direct anthropogenic emissions of Hg(II) are also tracked as separate tracers. The modeled processes, except for the boundary layer mixing process, are found to be linear, such that the sum of the concentrations of the tagged species is equal to the total Hg(II) concentration. We adjust for this non-linearity by constraining the sum of the tagged species to the total Hg(II) concentration in the boundary layer. This adjustment does not have a large effect on the results of the tagged simulation in the free troposphere, especially since most of the free tropospheric Hg(II) is produced by *in situ* oxidation of Hg(0).

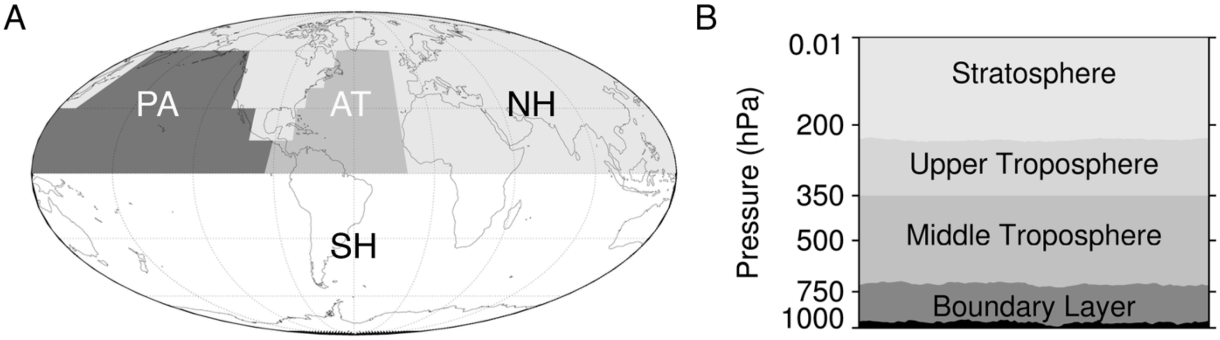

Figure 2.3. A map (A) and a cross-section (B) showing the horizontal and vertical extents of the tagged regions.

2.4.1 *Oxidation mechanism and sensitivity simulations*

The oxidation mechanism implemented in the earlier model versions (*Selin et al., 2007*) included slow oxidation of Hg(0) by OH and O_3 based on reaction rates observed in the laboratory-based studies of Hall et al. (*1995*) and Sommar et al. (*2001*). As an alternative to the OH/O_3 mechanism, Holmes et al. (*2010*) implemented the two-step Br-induced oxidation mechanism to GEOS-Chem, based on the work of Goodsite et al. (*2004*), Donohoue et al. (*2006*), and Balabanov et al. (*2005*). The reaction rates for R1 and R2 have been updated following the findings of Dibble et al. (*2012*) and Goodsite et al. (*2012*). Holmes et al (*2010*) had assumed Br and OH as the second-step oxidants in reaction R4. I have included, in addition, BrO, HO_2, and NO_2 as the second-step oxidants, following the recommendations of Dibble et al. (*2012*). The reaction mechanism is summarized below:

$$\mathrm{Hg(0) + Br \overset{M}{\rightarrow}\ HgBr} \qquad \text{(R1)}$$

$$\mathrm{HgBr \overset{M}{\rightarrow}\ Hg(0) + Br} \qquad \text{(R2)}$$

$$\mathrm{HgBr + Br\ \rightarrow Hg(0) + Br_2} \qquad \text{(R3)}$$

$$\mathrm{HgBr + X\ \rightarrow\ Hg(II)\ \ (X = OH, Br, BrO, HO_2, NO_2)} \qquad \text{(R4)}$$

The rates for the above reactions are:

$$k_1 = 1.46\times10^{-32}\times\left(\frac{T}{298}\right)^{-1.86}\times[M]\ cm^3molecule^{-1}s^{-1} \tag{2.1}$$

(*Donohoue et al., 2006*)

$$k_2\ = 2.67\times10^{41}\times exp\left(\frac{-7292}{T}\right)\times\left(\frac{T}{298}\right)^{1.76}\ \times k_1\ \ s^{-1} \tag{2.2}$$

(*Goodsite et al., 2012*)

$$k_3 = 3.9\times10^{-11}\ cm^3molecule^{-1}s^{-1} \tag{2.3}$$

(*Balabanov et al., 2005*)

$$k_4 = 2.5\times10^{-10}\times\left(\frac{T}{298}\right)^{-0.57}\ cm^3molecule^{-1}s^{-1} \tag{2.4}$$

(*Goodsite et al., 2004; Dibble et al., 2012*)

Assuming the HgBr intermediate to be short-lived, we can derive the effective production rate of Hg(II) as follows:

$$\mathrm{P}(\mathrm{Hg(II)}) = [\mathrm{Hg(0)}]k_{\mathrm{eff}} \tag{2.5}$$

$$k_{\mathrm{eff}} = \left(\frac{k_1k_4[Br][X]}{k_2+k_3[Br]+k_4[X]}\right)\ cm^3molecule^{-1}s^{-1} \tag{2.6}$$

If X includes only OH and Br, k_{eff} at the surface is low (~1.2×10^{-9} s^{-1}) because warm temperatures lead to rapid thermal dissociation of HgBr (reaction R2) and Br concentrations are lower ($2\text{-}5\times10^{5}$ molecule cm^{-3}) , but increases by about two orders of magnitude in the upper troposphere (10-12 km), where temperatures are low and Br radicals are abundant (1×10^{6} molecule cm^{-3}). When BrO, HO_2, and NO_2 are also included in X, reaction R4 is faster by 2-3 orders of magnitude and becomes the dominant pathway for loss of HgBr. This significantly decreases the vertical gradient in k_{eff}(surface: ~1×10^{-7} s^{-1} ; 10-12 km:~5×10^{-7} s^{-1}).

The standard ('Std') simulation follows the Br oxidation mechanism described above. We perform additional sensitivity simulations to gauge the effect of uncertainties in the oxidation kinetics. The two sensitivity simulations increase P(Hg(II)) by either tripling Br concentration ('3xBr') or using a faster k_1 rate constant ('FastK'). Each of these simulations is described below.

A large source of uncertainty in the oxidation process is the concentrations of Br in the troposphere. Our understanding of the sources of Br and the heterogeneous cycling between bromine species is incomplete (*von Glasow et al., 2004*). The two largest sources of bromine to the free troposphere are sea-salt debromination and the emission of organobromide species from oceanic phytoplankton (*von Glasow et al., 2004; Yang et al., 2005*), both of which have large uncertainties. The heterogeneous reactions between the bromine reservoir species, HBr and HOBr, are important for recycling of BrOx in the free troposphere (*von Glasow et al., 2004*), but the kinetics of these reactions in the atmosphere are uncertain as well (*Abbatt et al., 2012*).

In situ observations of BrO in the free troposphere are too scarce to provide adequate constraints on the modeled processes. Alternatively, global models have been evaluated using satellite-based observations of BrO. But, satellite-based estimates of tropospheric BrO column densities themselves carry large uncertainties. These arise from the interference of clouds and high-albedo surfaces, and from the procedure used to quantity the stratospheric mass of BrO (*Theys et al., 2011*). The GEOS-Chem simulated tropospheric column densities of BrO agree well with the GOME-2 satellite data in the polar regions (>60°), but are underestimated elsewhere, by an average of 40% (*Parrella et al., 2012*). In both the tropics and the mid-latitudes, the simulated values lie within the uncertainty of the observations, but, in the tropics, are lower than the best estimate by a factor of 2-4 throughout the year (*Figure 5 of Parrella et al., 2012*). A comparison with aircraft-based measurements of BrO in the Equatorial South Pacific found that the GEOS-Chem's results were low by a factor of 2.4-2.9 (*Rainer Volkamer, University of Colorado, unpublished results*). During the NOMADSS campaign as well, high BrO concentrations of 1.9 pptv were observed at the 7 km altitude over Texas (*Gratz et al., 2015*). These were a factor of four higher than the concentrations simulated by the GEOS-Chem model.

To assess the effect of the possible underestimate in BrO concentrations on to the Hg(II) concentrations, I perform a sensitivity simulation in which the Br concentrations were increased by a factor of three in the 45°S to 45°N latitude band between 750hPa and the tropopause. This simulation is denoted in this study as the '3xBr' simulation.

The rate constant for the atom-atom recombination reaction of Hg(0) with Br (Reaction R1) has been reported in several studies, in addition to those cited above. These studies are based on both laboratory measurements and theoretical computations, and the range of their estimates of the rate constant is about an order of magnitude wide. Laboratory-based measurements place the rate constant between 3.6×10^{-13} (± 50% uncertainty) (*Donohoue et al., 2006*) and 3.2×10^{-12}

cm^3 $molecule^{-1}$ s^{-1} (*Ariya et al., 2002*) at STP (298.15 K; 1 atm). This difference arises mainly from the differences in measurement techniques employed in these studies (*Subir et al., 2011*). The rate constants derived from theoretical calculations also vary greatly: 3.6×10^{-13} (*Goodsite et al., 2012*), 9.8×10^{-13} (*Shepler et al., 2007*), and 2×10^{-12} cm^3 $molecule^{-1}$ s^{-1} at STP (*Khalizov et al., 2003*).

The 'Std' simulation uses the rate constant reported by Donohoue et al. (*2006*). This is in remarkable agreement with the value reported by Goodsite el al. (*2012*), but is the lowest of all the other estimates. My second sensitivity simulation assesses the effect of the uncertainty in the magnitude of the oxidation rate constant. I use the oxidation rate constant measured by Ariya et al (*2002*), which is the largest of all the estimates. Following Dibble et al. (*2012*), the rate constant for the backward reaction (Reaction R2) is increased, such that its equilibrium constant with the forward reaction (reaction R1) is maintained at the value. This sensitivity simulation is denoted as the 'FastK' simulation here.

For both the sensitivity simulations, the reduction rate is increased such that the tropospheric burden of THg remains close (within 5%) to the burden of THg simulated by the 'Std.' model. It is important to note that the uncertainties in the modeled atmospheric burden of THg, its emissions, and lifetime are larger than 5% (*Selin, 2009*). The purpose of maintaining the THg burden in the sensitivity simulations is only to isolate the effect of faster oxidation on the simulated Hg(II) concentrations.

For each of the three simulations, I run the 4°×5° global mercury model with a spin-up period of three years to generate the boundary conditions for the nested-domain, and to calculate the annual global mercury budget. Next, for the three simulations, I run the 0.25°×0.3125° mercury model for North America from June 1 to July 15, 2013. For comparison to the NOMADSS aircraft observations, the model is sampled along the flight track at the 2.5-minute time step of the UW-DOHGS instrument.

Chapter 3. RESULTS AND DISCUSSION

3.1 OBSERVED DISTRIBUTION OF THG AND HG(II)

The UW-DOHGS instrument was operational during all nineteen flights of the campaign, and concentrations of THg were measured continuously during each flight. Although THg was measured at all times during the campaign, its speciation could be determined only about half of the time. The coverage of the speciated measurements was particularly low in the moist boundary layer, where the high amounts of water vapor reduced the retention efficiency of the Hg(II) filter. Speciation could also not be determined during the periodic calibration cycles in the 'same air' configuration (Section 2.2). Many observations were made in plumes downwind of point pollution sources, such as coal-fired power plants (*Ambrose et al., 2015*), and I exclude these measurements from our analysis. I assume that an air sample is part of a plume when concentrations of NO_x, SO_2, or C_3H_8 exceed 2 ppbv. This eliminates 6% of the THg and 4% of the Hg(II) measurements from this analysis. We further exclude about 1% of the observations where the flight coordinates were not recorded due to a temporary fault in the onboard data system. The maps and vertical profiles of the observed concentrations of THg and Hg(II) during the campaign are presented in Figures 3.1 and 3.2.

The mean and standard deviation of the observed THg concentrations was 1.49 (±0.16) ng/m^3. The concentrations of THg decrease slightly with altitude, from a mean of 1.54 ng/m^3 near the surface to 1.42 ng/m^3 at 7 km altitude. The variability in THg concentration is small, with the standard deviations at different levels ranging from 6 to 15% of the respective mean concentrations. The weak vertical gradient and the low standard deviation of the THg concentrations are consistent with the long tropospheric lifetime of THg. The observed vertical profile is also in agreement with the previous aircraft-based measurements of THg over North America (*Talbot et al., 2007; Swartzendruber et al., 2009; Mao et al., 2010*).

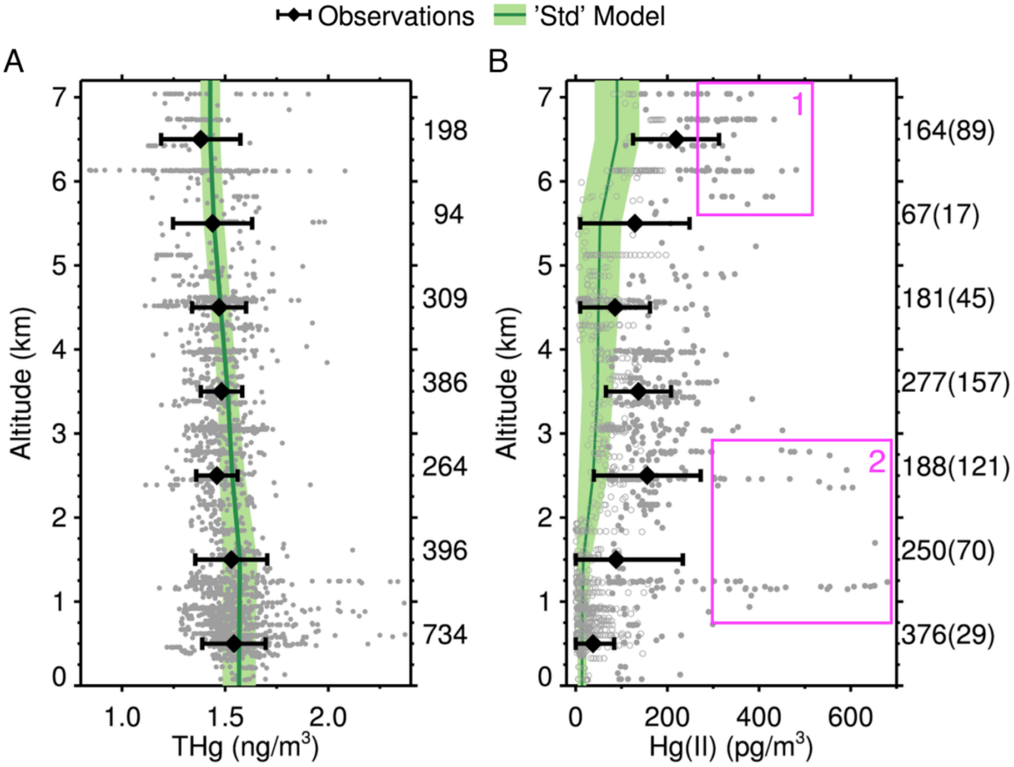

Figure 3.1. Vertical profiles of observed and 'Std' model concentrations of THg (A) and Hg(II) (B) during NOMADSS. Each observation above the LOD (limit of detection) is denoted by grey dots. Hg(II) observations below the LOD are shown as open circles and are estimated using the ROS (regression on order statistics) method. The means and standard deviations calculated for 1 km high vertical bins are shown (observations: black error bars, model: green line and shading). The numbers on the right hand side of each panel indicate the number of 2.5-min observations in each 1 km bin. The areas marked as '1' and '2' highlight measurements of high Hg(II) concentrations and are referenced in the text and Figure 3.2.

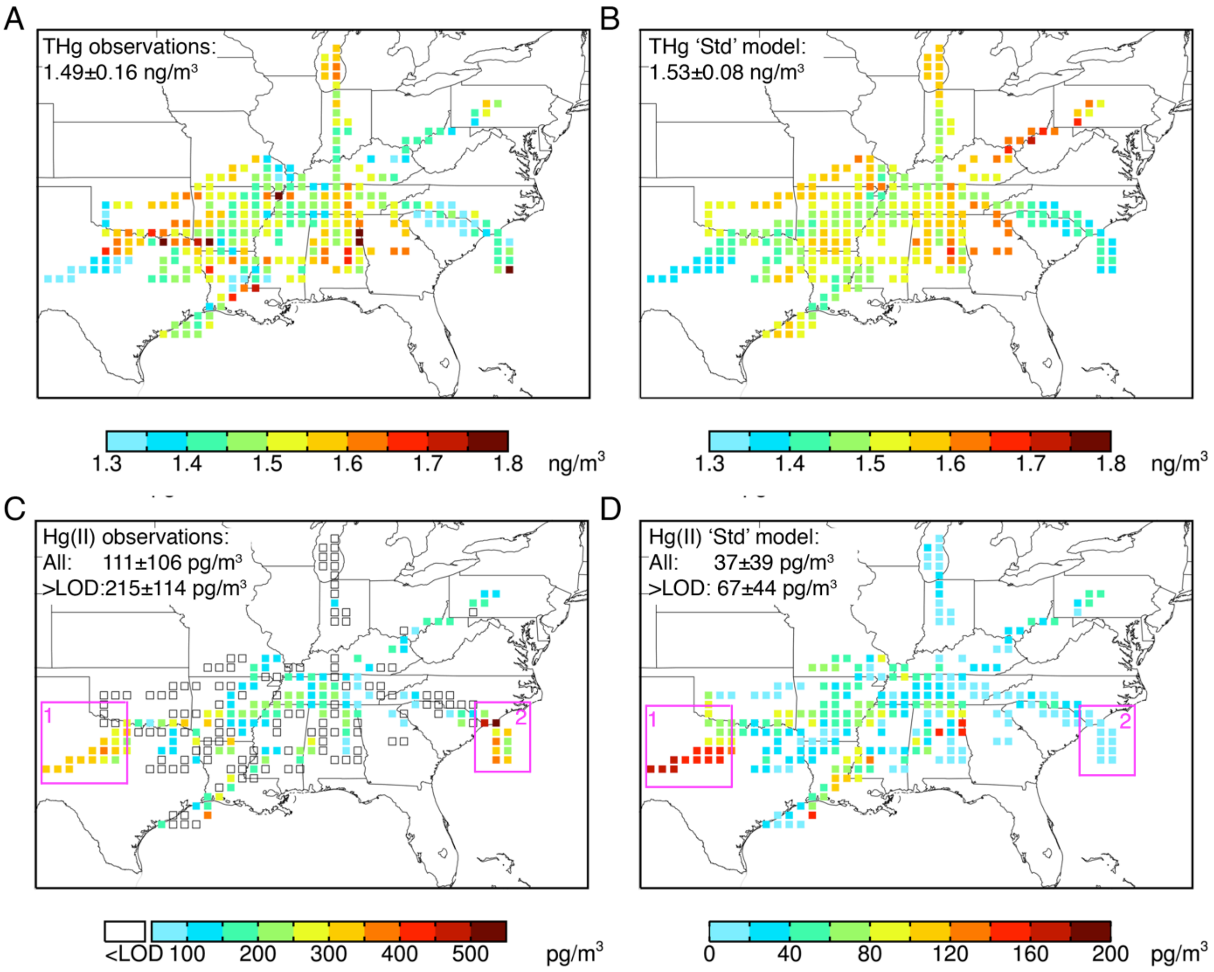

Figure 3.2. Maps showing the distribution of the observed (A) and 'Std' model (B) concentrations of THg, and of the observed (C) and 'Std' model (D) concentrations of Hg(II). For all four maps, the observed and simulated values are binned in 0.5° latitude by 0.625° longitude bins, and the mean value for the column is displayed. The means and the standard deviations are calculated from the individual observations and ROS estimates for observations below LOD. Hg(II) concentrations below LOD are shown by open squares. Note the different color scales for the observed (c) and simulated (d) values of Hg(II). Regions marked as '1' and '2' highlight the areas with high Hg(II) and are referenced in the text and in Figure 3.1.

Near the surface, high THg concentrations (exceeding 2 ng/m^3) were observed not only close to large emission sources, especially in Texas and Alabama, but also away from emission sources in the marine boundary layer of the Atlantic Ocean. An analysis of the THg distribution near land and ocean surfaces is presented by Song et al. (*manuscript in preparation*). In the free troposphere, THg concentrations higher than 1.75 ng/m^3 were found in air masses influenced by anthropogenic emissions (mean concentrations of CO and NO$_x$ of 117 ppbv and 275 pptv, respectively). THg concentrations of less than 1.2 ng/m^3 were associated with low concentrations of CO (mean of 64 ppbv) and NO$_x$ (mean of 111 pptv).

Compared to THg (2352 2.5 min sampling points), there were fewer observations of Hg(II) (1475 points), because Hg(II) was not measured during calibration cycles, and because of water vapor interference, particularly in the boundary layer (see section 2.2). Out of the 532 observations of Hg(II) in the boundary layer, 463 (87%) were below the instrument's LOD (non-detects). In the free troposphere, 502 (54%) out of the 943 observations were non-detects. Hg(II) observations below the LOD are shown with open circles and squares in Figures 3.1 and 3.2. I use the robust Regression on Order Statistics (ROS) method to impute values below the LOD and calculate the means and standard deviations (*Helsel, 2011*). The ROS method assumes a lognormal distribution for the observations, and estimates the distribution's parameters using the measurements above the LOD. The values below the LOD are then estimated using the fitted distribution. Helsel (*2011*) recommends the ROS method over the conventional substitution methods when more than half of the measurements are non-detects. The ROS method assumes a lognormal distribution for the observations, and estimates the distribution's parameters using the measurements above the LOD. The values below the LOD are then estimated using the fitted distribution. When calculating the vertical profile of Hg(II) (Figure 3.1B), I apply the ROS procedure to observations in each 1 km vertical bin.

The mean value of the observed Hg(II) concentrations, including the non-detects, was 111 (± 106) pg/m^3 (Figure 3.1C). The mean value of the Hg(II) observations above LOD (35% of the observations) was 215 (± 114) pg/m^3. Hg(II) concentrations were higher in the free troposphere than in the boundary layer (Figure 3.1B). The mean concentration of Hg(II), with the non-detects included, was 142 (± 114) pg/m^3 in the free troposphere, while that in the boundary layer it was 42 (± 61) pg/m^3. These observations of Hg(II) during NOMADSS are similar to previous observations of Hg(II). During five summertime flights in the Pacific Northwest, Swartzendruber et al. (*2009*) found RGM (gaseous component of Hg(II)) to be generally below their instrument's LOD of 80-160 pg/m^3. Mean Hg(II) concentrations of 48 pg/m^3 were measured at the high elevation Mt. Bachelor Observatory (2.7 km a.s.l.) in Oregon during the spring and summer of 2005 (*Swartzendruber et al., 2006*). Higher concentrations of Hg(II) in the free troposphere than in the boundary layer were observed by Swartzendruber et al. (*2009*) and Sillman et al. (*2007*), too.

During NOMADSS, large enhancements in Hg(II) were seen over Texas (marked as box 1 in Figures 3.1 and 3.2) and over the Atlantic Ocean near South Carolina (marked as box 2). Hg(II) concentrations of up to 500 pg/m^3 were observed between altitudes of 5 and 7 km during two flights (RF-06 and RF-09) over Texas. Concentrations of up to 680 pg/m^3 were observed between 1 and 3 km during one flight (RF-16) over the Atlantic Ocean. Although not typical, such high concentrations of Hg(II) have previously been observed in air masses of upper tropospheric origin at the Mt. Bachelor Observatory (*Swartzendruber et al., 2006*) and at Mauna Loa, Hawaii (*Landis et al., 2005*). The details of these flights are presented in section 3.5, and are also discussed by Gratz et al. (*2015*).

High elevation ground-based and aircraft-based measurements have shown that high free tropospheric Hg(II) concentrations were observed in air masses that were dry and clean (*Landis et al., 2005; Swartzendruber et al., 2006; Fain et al., 2009; Swartzendruber et al., 2009; Sheu et al. 2010*). To examine whether this relation holds for the NOMADSS observations too, we classify all THg and Hg(II) observations based on the measured relative humidity (RH) and CO concentrations averaged over the 2.5 minute time interval of the THg measurements (Table 3.1). A similar classification system based on water vapor mixing ratios and CO concentrations was used to identify air masses during CalNEX 2010 campaign (*Neuman et al., 2012*). I use thresholds of 35% for RH and 75 ppbv for CO to classify the observations into four categories: 'high RH/high CO', 'high RH/low CO', 'low RH/high CO' and 'low RH/low CO'. When RH or CO measurements were missing (18% of the observations), the GEOS-Chem simulated RH and CO concentrations have been used, instead, for the classification.

Using this method, I find that most of the observations (69% of the THg observations) were in the 'high RH/high CO' category. Most of these measurements were made in the continental boundary layer, and were characterized by high concentrations of CO (126 ppbv), CH_2O (2.7 ppbv), NO_x (230 pptv), and O_3 (54 ppbv). The mean concentration of THg was 1.53

ng/m^3, while that of Hg(II) was 48 pg/m^3 (156 pg/m^3 for observations > LOD, 14% of the observations). The ROS procedure is used to impute the non-detects, but the empirical distribution is now calculated separately for each category. Compared to the 'high RH/high CO' samples, the 'high RH/low CO' samples (8% of the observations) had lower CO (66 ppbv), CH_2O (0.8 ppbv), NO_x (42 pptv), and O_3 (44 ppbv). These samples were observed mostly near the marine boundary layer during the two flights over the Atlantic Ocean, but some were observed at high altitudes possibly in air detrained from clouds. The mean concentration of THg was 1.44 ng/m^3, and that of Hg(II) was 122 pg/m^3 (250 pg/m^3 for observations > LOD, 33% of the observations). The mean Hg(II) concentrations excluding the non-detects in the 'high RH/low CO' category was high because a few of the high Hg(II) concentrations seen during the Atlantic flight RF-16 were categorized as 'high RH/low CO', although most of them were categorized as 'low RH/low CO'.

About 24% of the Hg observations were classified as 'low RH/high CO'. These air samples were observed on all flights, particularly during the free tropospheric transit legs. The mean concentrations of CO, CH_2O, NO_x, and O_3 in these samples were 103 ppbv, 0.7 ppbv, 70 pptv, and 63 ppbv, respectively. HYSPLIT backtrajectories (not shown) for most of the 'low RH/high CO' samples indicate descending southward transport of these air masses from the high-latitude mid- and upper-troposphere (6-12 km asl). The THg concentrations in the 'low RH/high CO' air masses averaged 1.49 ng/m^3, and the Hg(II) concentrations averaged 146 pg/m^3 (190 pg/m^3 for observations > LOD, 41% of the observations).

I find that 6% of the THg observations fall into the 'low RH/low CO' category. These air samples are characterized by the low concentrations of CO (66 ppbv), CH_2O (0.5 ppbv), NO_x (57 pptv), and O_3 (52 ppbv). These air samples were observed mainly during the high altitude (5-7 km) flights over Texas, but also close to the marine boundary layer (1-3 km altitude) during the Atlantic flights. The chemical characteristics and HYSPLIT backtrajectories for these 'low RH/low CO' air masses suggest subsidence from the clean upper troposphere. This air mass had the lowest THg concentrations (1.34 ng/m^3), and the highest Hg(II) concentrations (265 pg/m^3, 318 pg/m^3 for observations > LOD). The presence of high Hg(II) in dry air is consistent with the previous studies mentioned above. It suggests that Hg(II) concentrations are higher in the upper troposphere, where once produced by oxidation it accumulates due to slower loss by deposition.

Table 3.1.The chemical characteristics of the four air mass categories. The numbers presented are the means and standard deviation of the concentrations.

	All	low RH/ low CO[a]	low RH/ high CO[b]	high RH/ low CO[c]	high RH/ high CO[d]
No. of THg observations[e]	2352	199	566	185	1402
THg observations (ng/m^3)	1.49 ± 0.16	1.34 ± 0.15	1.49 ± 0.10	1.44 ± 0.21	1.53 ± 0.15
No. of Hg(II) observations[f] (>LOD)[g]	1475 (516)	160 (116)	422 (248)	140 (48)	753 (104)
Hg(II) all observations (> LOD) (pg/m^3)	111 ± 106 (215 ± 104)	265 ± 145 (318 ± 136)	146 ± 82 (190 ± 78)	122 ± 129 (250 ± 143)	48 ± 57 (156 ± 73)
No. of flights[h]	19	8	18	9	18
Altitude (km)	2.6 ± 1.9	4.7 ± 1.9	3.9 ± 1.2	2.7 ± 2.3	1.7 ± 1.5
RH (%)	51 ± 27	16 ± 11	16 ± 10	68 ± 17	66 ± 13
CO (ppbv)	113 ± 35	66 ± 4	103 ± 32	66 ± 3	126 ± 31
O_3 (ppbv)	57 ± 14	52 ± 16	63 ± 16	44 ± 16	54 ± 10
NO_x (pptv)	160 ± 179	57 ± 35	70 ± 36	42 ± 39	230 ± 168
CH_2O (ppbv)	1.7 ± 1.3	0.5 ± 0.3	0.7 ± 0.3	0.8 ± 0.3	2.7 ±1.3

a. RH ≤ 35% and CO ≤ 75ppbv, b. RH ≤ 35% and CO > 75ppbv,
c. RH > 35% and CO ≤ 75ppbv, d. RH > 35% and CO > 75ppbv,
e. Number of 2.5-minute averaged THg observations
f. Number of 2.5-minute averaged Hg(II) observations including non-detects
g. Number of 2.5-minute averaged Hg(II) observations above LOD
h. Number of flights where the air masses were encountered

3.2 STANDARD ('STD') GEOS-CHEM HG SIMULATION

The THg concentrations simulated by the 'Std' GEOS-Chem model (1.53 ± 0.08 ng/m^3) agree closely with the observations (1.49 ± 0.16 ng/m^3) (Figures 3.1A and B). The 'Std' model captures the decrease in THg concentrations observed over central Texas, South Carolina, and part of the Atlantic Ocean, but overestimates THg concentrations over the Ohio River Valley by ~20%. Overall, the simulated THg concentrations are within ±10% of the measured concentrations for most (70%) of the observations. The vertical profile of the GEOS-Chem simulated concentrations of THg with the 'Std' simulation agrees well with the observed vertical profile (Figure 3.1A). The mean simulated THg concentration near the surface is 1.58 ng/m^3 (observed: 1.54 ng/m^3) and decreases to 1.43 ng/m^3 (observed: 1.42 ng/m^3) at the 7 km altitude. The agreement in the simulated and observed vertical profiles of THg demonstrates the model's skill in simulating the mean lifetime of THg in the lower and middle troposphere over the Southeastern US. It also shows the accuracy of the model's estimate of the emissions of THg in the region. Despite the good agreement with the observed mean THg values, the 'Std' model displays variability in THg that is a factor of 2 to 5 lower than the observed variability (Figure 3.1A).

The 'Std' model significantly underestimates the observed Hg(II) (Figures 3.1, 3.2 and Table 3.2). Compared to all (including <LOD) Hg(II) observations (111 ± 106 pg/m^3), the 'Std' model is a factor of three too low (37 ± 39 pg/m^3). When considering only observations above the LOD, the bias is even larger (model: 67 ± 44 pg/m^3, observations: 215 ± 114 pg/m^3). Either way, the simulated Hg(II) concentrations are found to be significantly too low compared to the observations. As seen in Figure 7, the 'Std' simulation has a large negative (-89 to -66%) normalized mean bias (NMB, NMB $= \sum(M_i - O_i)/\sum O_i \times 100$), and has a small fraction (1-51%) of data points where the 'Std' model is within a factor of two of the observations (FAC2, fraction of points where the model is within a factor of two of the observations or $0.5 \leq M_i/O_i \leq 2$).

Despite this overall underestimate, the 'Std' model qualitatively reproduces the horizontal variability in Hg(II) (Figure 3.1C and D, note the different color scales), as well as the increase in Hg(II) concentrations with altitude (Figure 3.1B). Furthermore, the 'Std' model captures the factor of 3-6 enhancement in Hg(II) for the 'low RH' air masses relative to the 'high RH' air masses (Tables 3.1 and 3.2).

Table 3.2. Modeled THg and Hg(II) concentrations in the three simulations for the four air mass categories. The numbers presented are the means and standard deviation of the concentrations.

	All	low RH/ low CO	low RH/ high CO	high RH/ low CO	high RH/ high CO
Hg(II) all observations (> LOD) (pg/m^3)	111 ± 106 (215 ± 104)	265 ± 145 (318 ± 136)	146 ± 82 (190 ± 78)	122 ± 129 (250 ± 143)	48 ± 57 (156 ± 73)
Std. Model Hg(II) (pg/m^3) all observations (> LOD)	37 ± 39 (67 ± 44)	87 ± 54 (89 ± 58)	63 ± 36 (64 ± 32)	12 ± 17 (9 ± 15)	20 ± 20 (23 ± 16)
3xBr Model Hg(II) (pg/m^3) all observations (>LOD)	44 ± 59 (80 ± 87)	136 ± 102 (163 ± 119)	74 ± 55 (76 ± 61)	16 ± 24 (12 ± 19)	22 ± 31 (27 ± 22)
FastK Model Hg(II) (pg/m^3) all observations (>LOD)	56 ± 78 (98 ± 107)	167 ± 137 (184 ± 157)	104 ± 78 (102 ± 75)	13 ± 18 (11 ± 15)	27 ± 36 (28 ± 22)
THg Observations (ng/m^3)	1.49 ± 0.16	1.34 ± 0.15	1.49 ± 0.10	1.44 ± 0.21	1.53 ± 0.15
Std. Model THg (ng/m^3)	1.53 ± 0.08	1.43 ± 0.05	1.51 ± 0.05	1.41 ± 0.03	1.56 ± 0.07
3xBr Model THg (ng/m^3)	1.49 ± 0.11	1.37 ± 0.07	1.48 ± 0.07	1.33 ± 0.04	1.53 ± 0.10
FastK Model THg (ng/m^3)	1.49±0.09	1.39 ± 0.05	1.48 ± 0.05	1.36 ± 0.03	1.52 ± 0.08

Considering that (i) previous studies have demonstrated the model's skill in predicting ambient concentrations and deposition of mercury species at the surface, (ii) the model agrees with the NOMADSS observations for THg, RH, CO, NO_x, O_3, and CH_2O, and (iii) the model underestimates Hg(II) particularly in dry air masses where reduction is suppressed, I hypothesize that the bias in the Hg(II) concentrations is because the model simulated oxidation rate of Hg(0) is too slow. To test this hypothesis, I examine the sensitivity of the model results to the oxidation rate in two additional (sensitivity) simulations (Section 2.4.1). In the '3xBr' simulation, I evaluate the model's response to an increase in Br concentrations, and in the 'FastK' simulation, I evaluate the model's response to a higher oxidation rate constant.

3.3 RESULTS OF THE SENSITIVITY STUDIES

A summary of the modeled THg and Hg(II) concentrations for the sensitivity simulations is presented in Table 3.2. Figure 3.3 shows the vertical profiles of THg and Hg(II) for the 'Std' and the '3xBr' and 'FastK' simulations. All three GEOS-Chem simulations reproduce the observed mean THg and its vertical profile. The consistency of the '3xBr' and 'FastK' models with the 'Std' model is maintained by increasing the reduction rate's scaling coefficient to balance the increase in the oxidation rates, maintaining the overall burden of THg in the atmosphere (Section 2.4.1).

The largest increase in Hg(II) concentrations is in the 'low RH/low CO' category. Hg(II) concentrations for this category increase to 136 ±102 pg/m^3 ('3xBr'), and to 167 ± 137 pg/m^3 ('FastK') from 87 ± 54 pg/m^3 ('Std'). Although still lower than observations (265 ± 145 pg/m^3), the model bias decreases considerably. The NMB, considering only observations above the LOD, for the 'low RH/low CO' category decreases from -72% in the 'Std' model to -48% and -42% in the '3xBr' and 'FastK' models, respectively (Figure 3.4A-C), and the FAC2 increases from 24% in the 'Std' model to 61% in the '3xBr' and 55% in the 'FastK' simulations.

The high Hg(II) measurements in this category that do not show any change with the '3xBr' and 'FastK' models were the ones made during flight RF-16. The details of this flight are presented in section 3.5. The improvement in the model performance is also reflected in the vertical profile of Hg(II) in Figure 3.3B. The '3xBr' and 'FastK' models show better agreement with the observations between the altitudes of 5 and 7 km. This altitude range is where most of the 'low RH/low CO' air samples were observed, particularly during flights RF-06 and RF-09.

In the 'low RH/high CO' category, the '3xBr' simulation shows no improvement over the 'Std' model. The mean '3xBr' Hg(II) concentration (74 ± 55) pg/m^3 is similar to that of the 'Std' (63 ± 36 pg/m^3), and significantly lower than the observed concentrations (146 ± 82 pg/m^3). In the 'FastK' simulation, the Hg(II) concentrations increase to 104 ± 78 pg/m^3, with an improvement in the NMB ('FastK': -45%, '3xBr':-60%, 'Std':-66%) (Figures 3.4 D-F). The lack of improvement with the '3xBr' model is because many of the 'low RH/high CO' air samples can be traced back to the high-latitudes. Since the '3xBr' model uses higher Br concentration only between 45°N and 45°S, the oxidation rates in the high-latitudes remained equal to that in the 'Std' simulation. Furthermore, the '3xBr' model uses a higher global reduction rate than the

‘Std’ simulation, and thus simulates lower Hg(II) concentrations in the high-latitudes than the ‘Std’ model. For the ‘FastK’ simulation the FAC2 index is higher (56%) compared to the ‘Std’ (22%) and ‘3xBr’ (30%) simulations.

Due to the large fraction of non-detects, a comparison of the model performance with respect to the averages for the ‘high RH/low CO’ and ‘high RH/high CO’ categories is unreliable. For these categories, the ‘3xBr’ and the ‘FastK’ simulations show little improvement over the ‘Std’ model with respect to the Hg(II) concentrations. When considering only Hg(II) observations above the LOD, the NMB for the three model simulations is -80-96%, and the FAC2 is 1-8% (Figures 3.4G-L). When Hg(II) observations below the LOD are also considered, the NMB for the three simulations reduces to -71 to -64%, and the FAC2 increases to 14-29%.

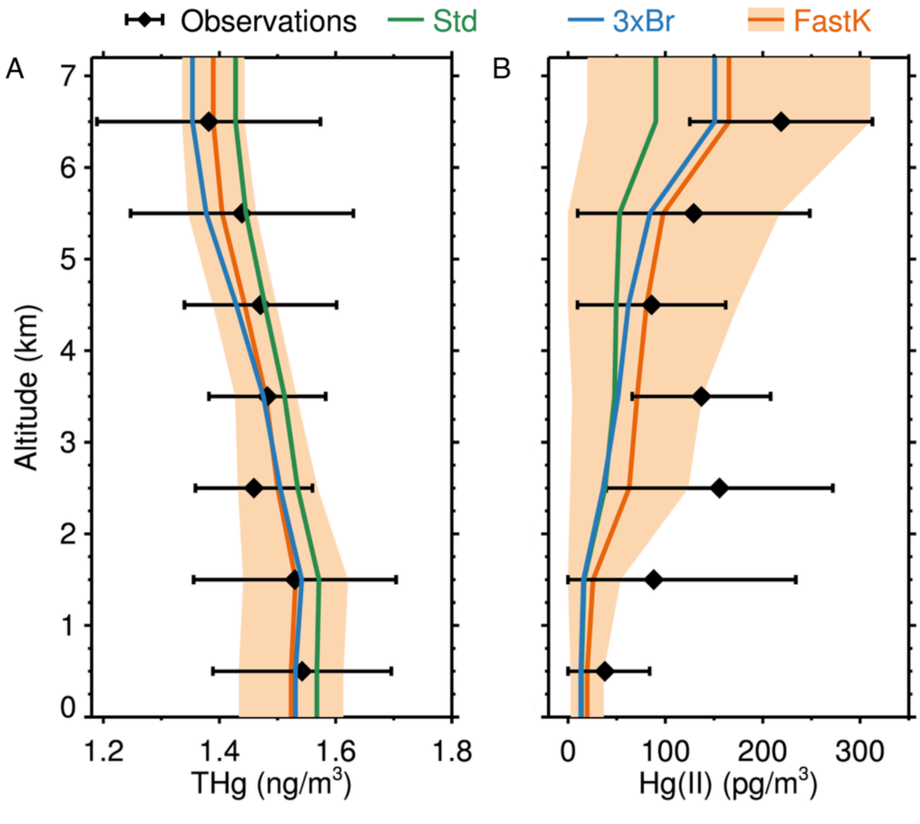

Figure 3.3. Vertical profiles of the observed concentrations of THg (A) and Hg(II) (B), and modeled concentrations with the ‘Std’ (green), ‘3xBr’ (blue), and ‘FastK’ (orange) model simulations. The means and standard deviations are shown (observations: black bars, ‘FastK’: orange shading). Hg(II) observations below LOD are estimated using the ROS method for each vertical bin.

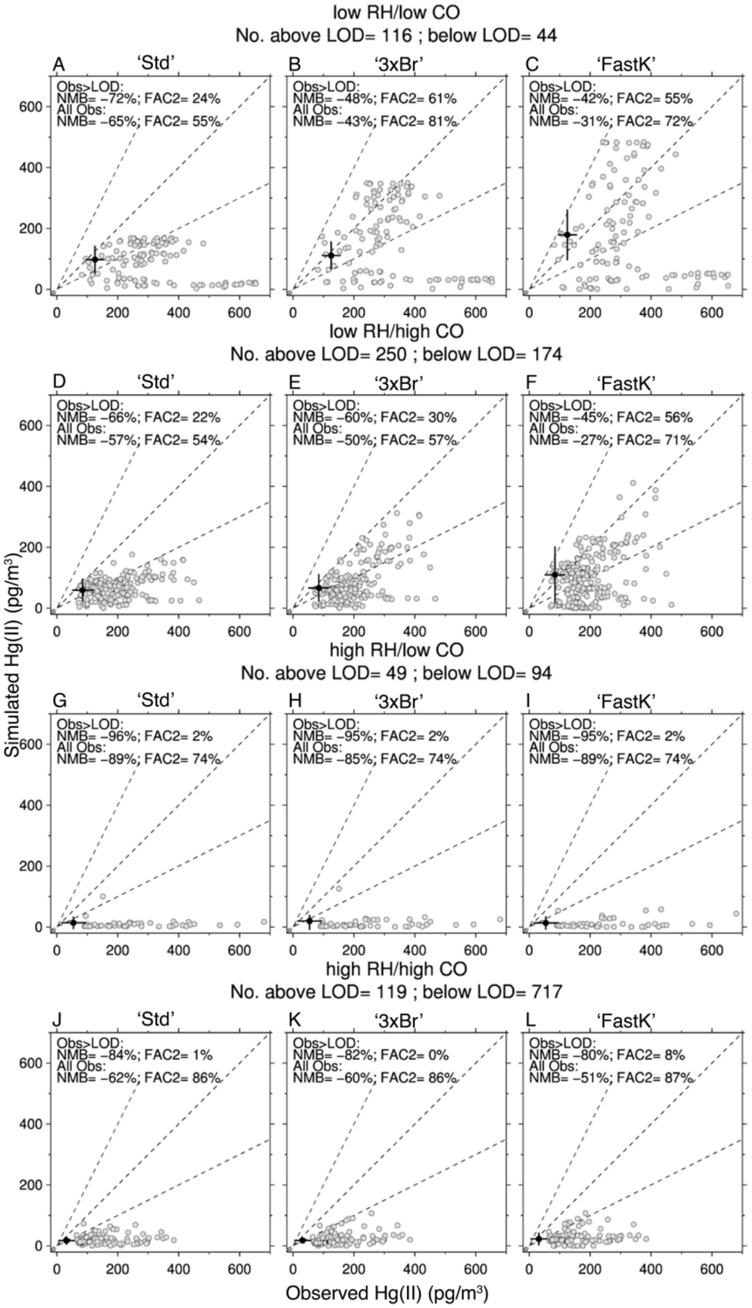

Figure 3.4. A comparison of the individual observations and simulated concentrations of Hg(II) with the three model simulations in the low RH/ low CO (A-C), low RH/ high CO (D-F), high RH/ low CO (G-I) and high RH/ high CO (J-L) categories. NMB is the normalized mean bias calculated as $\sum(M_i - O_i)/\sum O_i \times 100$, where O_i and M_i are observed and simulated values, respectively. FAC2 is the fraction of the samples where the simulated value is within a factor of 2 of the observations, or $0.5 \leq M_i/O_i \leq 2$. The black dots and lines represent the mean value

and standard deviation of the non-detects estimated with the ROS method for each air mass category separately, and that of the corresponding simulated concentrations.

The improved performance with the ‘3xBr’ and the ‘FastK’ simulations particularly for the ‘low RH/low CO’ air samples is evidence that the oxidation of Hg(0) is at least 3-5 times faster than what was considered previously in the model.

3.4 CAN OTHER OXIDANTS EXPLAIN THE HIGHER OXIDATION RATE?

The other possible oxidants for Hg(0) are O_3 (*Pal and Ariya, 2004a; Rutter et al., 2012*) and BrO (*Spicer et al., 2005; Raofie and Ariya, 2004*). I ran two additional simulations that include oxidation by O_3 and oxidation by BrO, respectively, in addition to the atomic Br-induced oxidation of the ‘Std’ model. The oxidation reactions included are:

$$\mathrm{Hg(0)} + \mathrm{O_3} \rightarrow \mathrm{Hg(II)} \qquad \text{(R5)}$$

$$\mathrm{Hg(0)} + \mathrm{BrO} \rightarrow \mathrm{Hg(II)} \qquad \text{(R6)}$$

With the Hg(0)+O_3 oxidation reaction included, the increase in the modeled Hg(II) concentrations occurs mostly in the continental boundary layer, and not in the subtropical upper troposphere, where most of the high Hg(II) air masses had originated. This suggests that the inclusion of the Hg(0)+O_3 reaction in the model cannot explain the observed Hg(II) enhancements.

When the Hg(0)+BrO oxidation pathway was considered in parallel to the ‘Std’ Hg(0)+Br oxidation pathway, the model simulated higher Hg(II) concentrations in the ‘low RH/low CO’ air masses, but not as high as the ‘3xBr’ and ‘FastK’ simulations. The NMB for >LOD observations in the ‘low RH/low CO’ category was -70%, compared to -48% for the ‘3xBr’ simulation and -42% for the ‘FastK’ simulation. Although including the Hg(0)+BrO reaction with the rate from Spicer et al. (*2005*) brings the model closer to the observations, it does not completely explain the model underestimate of Hg(II) concentrations.

3.5 CASE STUDIES FOR INDIVIDUAL FLIGHTS

I describe below in further detail the observations made during four NOMADSS flights. In three of the four flights unusually high concentrations of Hg(II) were observed. In the fourth flight, high concentration of Hg(II) were expected, based on meteorological forecasts of low RH, but were not observed. The timeseries of the observations and model results along the flight tracks are shown in Figures 3.5 and 3.6.

3.5.1 *Flight RF-06 (June 19, 2013)*

One of the goals of Flight RF-06 was to sample in dry air masses with potentially enhanced Hg(II) levels. The meteorological forecasts indicated the presence of such an air mass at high altitudes over west Texas. The flight plan was to make measurements in the boundary layer near Dallas, TX before sampling in this air mass. As soon as the plane started its ascent from Dallas, there was a distinct enhancement in the observed Hg(II) concentrations (Figure 3.5B). Between 17:57 and 19:40 UTC, at 6.8 km altitude, Hg(II) concentrations of 150-400 pg/m^3 were detected. The mean concentration of THg in this air mass was 1.35 ng/m^3, about 20% lower that the THg concentrations measured during the rest of the flight (Figure 3.5A). The observed (Figure 3.5C) low RH (11%), CO (65 ppbv), O_3 (39 ppbv), NO_x (53 pptv), CH_2O (204 pptv), and C_3H_8 (36 pptv) indicate a clean air mass. In addition, high concentrations of BrO (1.9 pptv) were observed in the air mass (*Gratz et al., 2015 submitted*). 7-day HYSPLIT backtrajectories (not shown here) indicate that the air mass was transported from the subtropical Pacific anticyclone 3 days before it was sampled over TX (*Gratz et al., 2015 submitted*). The backtrajectories show subsidence of the air mass from the upper troposphere (10-12 km) for at least 4 days before transport out of the Pacific anticyclone. The low concentrations of tracers of marine origin ($CHBr_3$: 0.86 ppbv, DMS: <LOD) in the air mass limit the likelihood of a recent influence from the marine boundary layer.

In the flight section where high Hg(II) concentration (271 pg/m^3) were observed, the mean Hg(II) concentration calculated by the 'Std' simulation (148 pg/m^3), was much lower than that for the '3xBr' (283 pg/m^3) and 'FastK' (289 pg/m^3) simulations (Figure 3.5B). The results of the 'tagged Hg(II)' simulation indicate that 60% of this Hg(II) was produced in the Pacific upper troposphere (above 10 km), and was subsequently transported over Texas (Figure 3.5D). In the upper troposphere, production of Hg(II) is high because of lower temperatures and higher concentrations of atomic Br. Furthermore, because removal of Hg(II) by deposition or reduction is slow, Hg(II) accumulates in the anticyclone. Outside the region with the high Hg(II) concentration, all three model simulations calculate Hg(II) concentrations that are below the instrument's LOD, in agreement with the observations.

3.5.2 *Flight RF-09 (June 24, 2013)*

Meteorological forecasts showed persistence of the dry air mass of subtropical Pacific origin over Texas, and on June 24, 2013 the objective of flight RF-09 was to resample this high-Hg(II) air over TX. Several measurements were made at an altitude of 6.7 km and, at five constant-altitude legs between 2.5 and 6.7 km. The THg concentrations showed large variations during the flight, with a range of 0.74 to 2.6 ng/m^3 (Figure 3.5E). The mean THg concentration for the entire flight, excluding the plumes (THg > 2 ng/m^3), was 1.46 ng/m^3. Higher concentrations of THg were associated with higher CO concentrations (Figure 3.5G). The mean CO concentration for samples with THg above the flight average was 99 ppbv, while that for THg samples below the flight average was 77 ppbv. High THg concentrations were again seen near large emission sources.

Concentration of Hg(II) varied between the LOD (95 pg/m^3) and 481 pg/m^3 (Figure 3.5F). The vertical profile of Hg(II) was nearly uniform, with the mean concentrations at each level ranging from 287 to 370 pg/m^3. The air mass with high Hg(II) concentrations encountered between 1600 and 1930 UTC had low RH (19%) and low O_3 concentrations (50 ppbv) (Figure 3.5G). Similar to the flight RF-06, the HYSPLIT backtrajectories show transport from the subtropical Pacific anticyclone. However, compared to the air mass observed in flight RF-06, this air mass had higher concentrations of THg (1.50 ng/m^3) and CO (85 ppbv). Even in the continental boundary layer, at an altitude of 1.2 km, the concentration of Hg(II) was as high as 359 pg/m^3. This was associated with high THg concentrations of about 2.0 ng/m^3, and was probably due to emissions of both Hg(II) and Hg(0) from nearby sources.

The mean THg concentrations for the flight calculated by all three simulations are between 1.38 and 1.42 ng/m^3, and are close to the mean of the observations. The mean Hg(II) concentrations for the flight section between 1600 and 1900 UTC simulated by the '3xBr' (199 pg/m^3) and 'FastK' (226 pg/m^3) simulations are closer to the observations (311 pg/m^3) than the

‘Std’ (106 pg/m^3) simulation. Between 1900 and 1930 UTC, the simulated concentrations for the three simulations (39-60 pg/m^3) are considerably lower than the observed concentrations (300 pg/m^3). The simulated RH (54%) during this time was higher than the observed RH (25%). This may be due to a model error in simulating transport or the boundary layer depth in this section of the flight. The results of the ‘tagged’ Hg(II) simulation show that about 50% of the high Hg(II) encountered during this flight was produced in the Pacific upper troposphere, in similarity to flight RF-06 (Figures 3.5D and 3.5H).

3.5.3 *Flight RF-10 (June 27, 2013)*

Flight RF-10 was the third flight planned to observe the Hg(II) concentrations at high altitudes over northern Texas and Oklahoma. High altitude observations between 4.6 and 6.1 km were made for a three-hour period (1520 to 1820 UTC), but throughout this period Hg(II) concentrations in all but one sample were below the instrument LOD of 134 pg/m^3 (Figure 3.6B). The mean value of THg, CO, and O_3 concentrations for 1520-1820 UTC was 1.51 ng/m^3, 83 ppbv, and 44 ppbv, respectively (Figures 3.6A and C). The air mass was more humid, with a mean RH of 39%, than that seen during the two other Texas flights (RF-06 and RF-09). HYSPLIT backtrajectories suggest that the air mass had experienced precipitation and uplift, from 2-4 km to 10-12 km, over the eastern and central Pacific Ocean about 6 days before it was sampled. The origin of part of this air mass in the lower troposphere, where production of Hg(II) is likely slow, and the efficient deposition of Hg(II) during precipitation can explain the low Hg(II) observed during this flight.

The Hg(II) concentrations calculated by the ‘Std’ (39 pg/m^3) and ‘3xBr’ (59 pg/m^3) models for the high-altitude sector between 1520 and 1820 UTC are also below the instrument’s LOD. Even in the ‘FastK’ simulation, except for the period between 1730 and 1830 UTC, the calculated Hg(II) concentrations fall below the LOD (Figure 3.6B). Although, this is the same region over TX where high Hg(II) was simulated by the ‘3xBr’ and ‘FastK’ models for flights RF-06 and RF-09, much lower Hg(II) concentrations are simulated for this flight. This is because the air mass originated closer to the surface, where Hg(II) production is slow, had experienced precipitation during uplift, leading to deposition of Hg(II), and had not travelled through the subtropical anticyclone. A comparison of this flight with the other two Texas flights, shows that the model is able to capture the variability in Hg(II) concentrations that is seen in the observations.

3.5.4 *Flight RF-16 (July 8, 2013)*

During flight RF-16, the aircraft flew to the Atlantic Ocean near the South Carolina coast, with the goal of measuring the vertical distribution of mercury over the ocean. Of the eight constant altitude legs flown over the Atlantic, four were in the free troposphere, in the altitude range of 1.0 and 4.5 km, and four were in the marine boundary layer (MBL). THg showed a slight decrease from the MBL (1.58 ng/m^3) to the top of the vertical profile (1.37 ng/m^3) (Figure 3.6E). Hg(II) was mostly lower than the LOD (91 pg/m^3) in the MBL, but was high in the free troposphere with a mean concentration of about 450 pg/m^3 (Figure 3.6F). The free-tropospheric air had low concentration of CO (65 ppbv) and low RH (33%). $CHBr_3$ concentration was about 1 pptv in the free tropospheric air, compared to about 2 pptv in the MBL. The low RH and $CHBr_3$ suggest that the free-tropospheric air had not been in contact with the MBL in its recent past. The HYSPLIT backtrajectories show the air circulating in the subtropical Bermuda anticyclone for at least one week prior to the measurements (*Gratz et al., 2015*).

The GEOS-Chem THg concentrations in the MBL (1.34-1.38 ng/m^3) are lower than the observations (1.58 ng/m^3) suggesting an underestimate in the ocean emission flux calculated in the model. None of the model simulations can capture the enhancements in Hg(II) observed between 1700 and 1815 UTC, and again between 1930 and 2015 UTC. The mean of Hg(II) concentrations measured during those two periods was 415 pg/m^3, much higher than that simulated by the ‘Std’ (14 pg/m^3), ‘3xBr’ (24 pg/m^3), and ‘FastK’ (33 pg/m^3) models. The reasons behind such a large discrepancy are not clear, but could result from an underestimate in both oxidation rate constant and bromine concentrations.

During the flight BrO concentrations could not be determined because of interference from clouds. The instrument’s LOD was 0.9 pptv, and the simulated BrO concentrations were 0.2-0.3 pptv. If the BrO concentrations in the model are constrained to 0.9 pptv in the free troposphere over the North Atlantic Ocean, the Br radical concentrations increase proportionally. When these higher Br concentrations are used in the ‘FastK’ model, the simulated Hg(II) concentrations along the flight track increases significantly to 205 pg/m^3. The modeled location of the pocket of dry air was displaced by 200 km east of its observed location during the flight.

The simulated Hg(II) concentrations in this pocket of dry air was close to the observed concentrations (~600 pg/m^3). It suggests that oxidation of Hg(0) was particularly high in this air mass.

The above comparison of the simulated Hg(II) concentrations with the NOMADSS observations shows that the Hg(0) oxidation rate based on the standard rate constants (*Goodsite et al., 2004; Goodsite et al., 2012; Donohoue et al., 2006*) and the GEOS-Chem calculated Br concentrations is too slow. Increasing the Br concentrations by a factor of 3 or considering the higher rate constants of Ariya et al. (*2002*) leads to significant improvement in the model results in the free troposphere. Since the high LOD of the UW-DOHGS instrument prevents accurate measurements in the boundary layer, where Hg(II) concentrations are low, the NOMADSS observations are not suitable for an evaluation of the faster oxidation scenarios in the boundary layer. However, some insights can be gained by reviewing previous studies that have evaluated Hg(0) oxidation kinetics in the tropical or mid-latitude boundary layer.

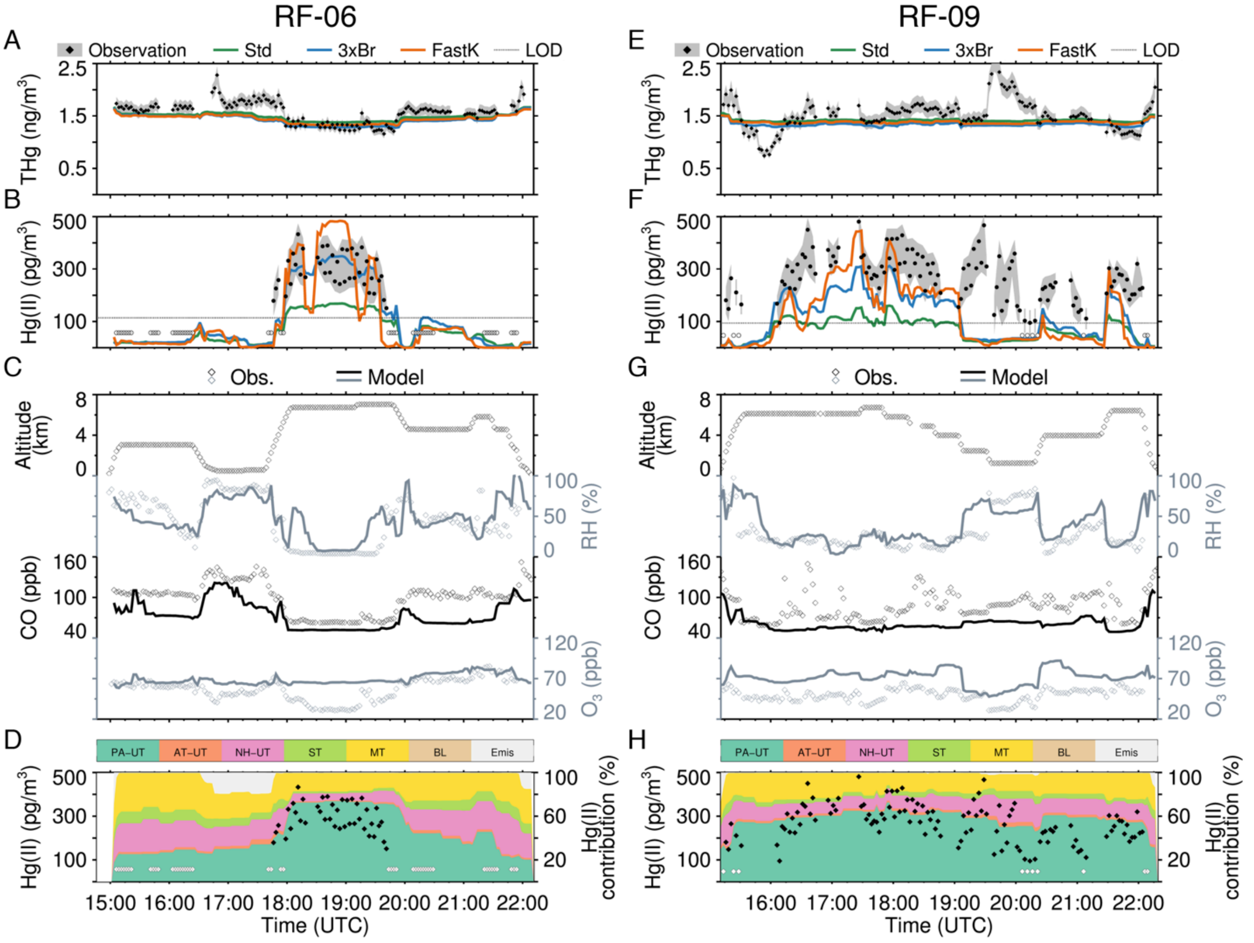

Figure 3.5. The timeseries of the observations of THg, Hg(II), altitude, RH, CO, and O_3 for flights RF-06 on 19 June (A-D) and RF-09 on 24 June (E-H). The THg and Hg(II) measurements are represented by filled diamonds with the uncertainty represented by the gray shading. The dashed line represents the LOD, and observations below the LOD are arbitrarily plotted at LOD/2 with open diamonds. Also shown (solid lines) are the simulated concentrations of THg and Hg(II) for the 'Std' (green), '3xBr' (blue), and the 'FastK' (orange) models. The flight altitude and observed concentrations of RH, CO, and O_3 are shown with open diamonds, and the simulated concentrations are shown with solid lines. The contribution of the simulated Hg(II) from different tagged regions in the 'Std' model is also displayed. Refer to Figure 2.3 for definition of the tagged regions.

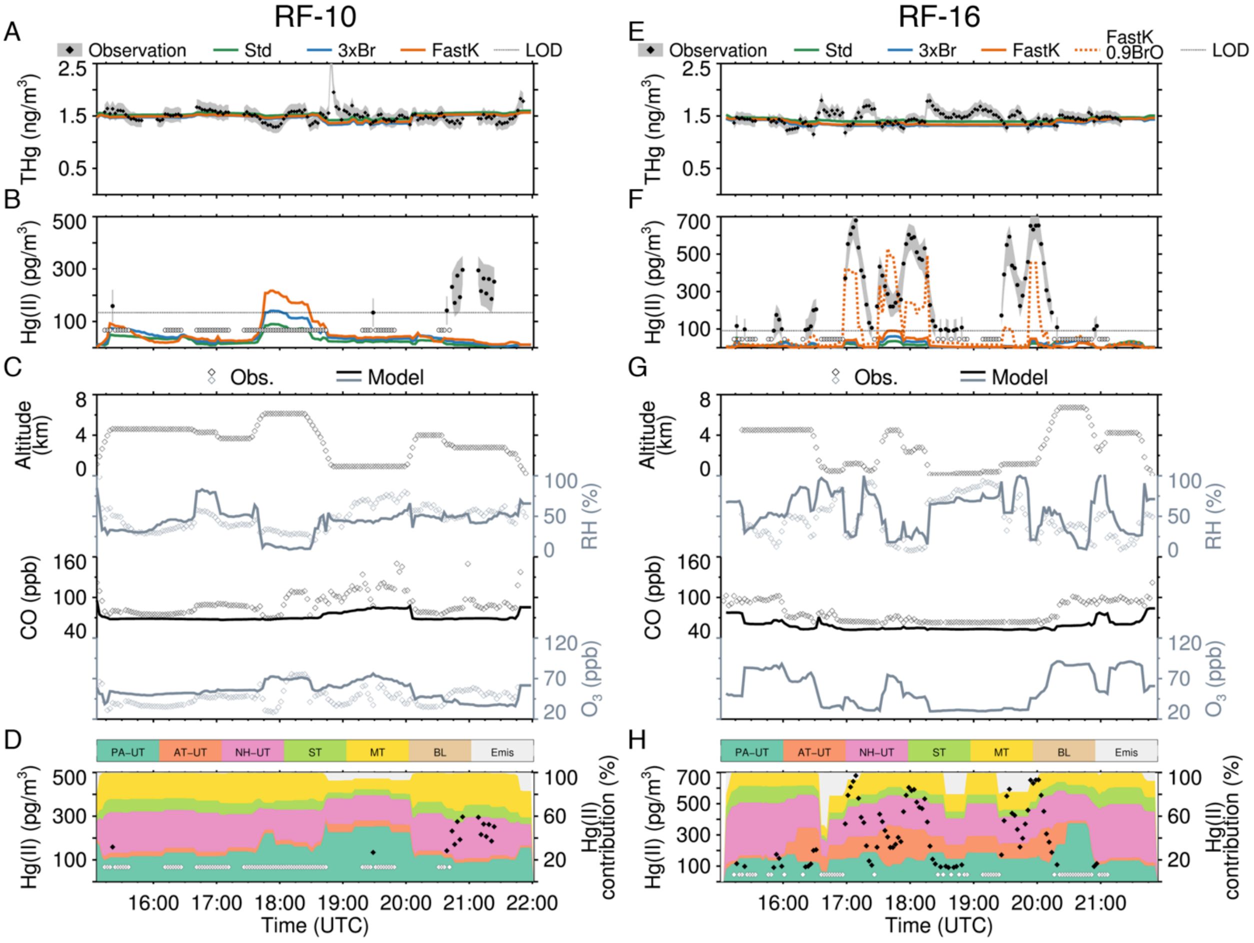

Figure 3.6. Same as figure 3.5, except for RF-10 (A-D) and RF-16 (E-H).

3.6 DISCUSSION OF OTHER OBSERVATION-MODELING STUDIES

Previous studies in the tropics and mid-latitudes have also reported that the standard Hg(0)+Br oxidation kinetics cannot reproduce the observed concentrations of Hg(II) (*Sprovieri et al., 2010a; Wang et al., 2014; Obrist et al., 2011; Tas et al., 2012*). All of these studies were based on measurements in the MBL, and used box models to interpret those observations. Sprovieri et al. (*2010a*) observed the diurnal variation in RGM concentrations in the MBL of the Adriatic Sea, and found enhancements at midday of 20-40 pg/m^3 due to *in situ* production of RGM. They tested several Hg(0) oxidation pathways in their box model to explain the observed RGM. They found that with the Hg(0)+ O$_3$ reaction (*Pal and Ariya, 2004a*) the modeled RGM built-up continuously over the simulation period and was an ~10 times higher than the observed nighttime minimum in RGM. They found that the Hg(0)+BrO (*Raofie and Ariya, 2004*) and the Hg(0)+OH (*Goodsite et al., 2004*) reactions were too slow and the model underestimated the observed midday RGM peaks by an order of magnitude. The best agreement with the RGM observations was found with the Hg(0)+Br reaction based on the higher oxidation rate of Ariya et al. (*2002*). But, they had to ignore the HgBr thermal dissociation reaction (Reaction R2, Section 2.4.1) to match the observations. This reaction was too fast in the typical summer temperatures and resulted in negligible RGM production in the MBL. This was despite the use of the lower thermal dissociation rate of Goodsite et al. (*2004*), which has since been revised upwards by two orders of magnitude (*Goodsite et al., 2012*). Sprovieri (*2010a*) considered Br as the sole second-step oxidant (reaction R4, Section 2.4.1). The inclusion of HO_2, NO_2, and BrO as second-step oxidants provides an additional pathway for the formation of RGM from HgBr (*Dibble et al., 2012*). Even at the high temperature of 30°C, a NO_2 concentration of 200 pptv is sufficient to make the second step oxidation reaction as fast as the HgBr dissociation reaction. This suggests that if these model calculations were to be repeated with the 'FastK' oxidation pathway, which includes the HgBr thermal dissociation reaction, the Hg(0) oxidation rate would be only about a factor of two lower than the rate simulated by Sprovieri et al. (*2010a*) by ignoring the HgBr thermal dissociation.

In a measurement (and modeling) study conducted over the Galapagos Islands in the equatorial Pacific, Wang et al., (*2014*) reached a similar conclusion regarding the importance of HO_2 and NO_2 in the Hg(0) oxidation close to the surface. They showed that the inclusion of HO_2 and NO_2 as second-step oxidants was necessary to simulate the observed magnitude of the mid-day peaks in RGM concentrations. This oxidation pathway is the same oxidation pathway used in this study's 'Std' model. However, Wang et al. (*2014*) further noted that because of the known bias in the Tekran's RGM measurement system, the observed RGM concentrations are likely several-fold lower than the actual concentrations. Thus, although their model concentrations matched the observations, they are possibly still lower than the actual Hg(II) concentrations. If the '3xBr' or the 'FastK' oxidation pathway were to be used instead, the production of RGM would increase by three-fold, and account for some of the bias between the observed and the actual concentrations of Hg(II).

Tas et al. (*2012*) present an analysis of mercury depletion events associated with extremely high BrO concentrations (20-80 pptv) over the Dead Sea in Israel. They investigated several oxidants using a box model and, in similarity to our study, found that the slow Br-oxidation kinetics was insufficient to reproduce the rate of depletion of Hg(0). They showed that oxidation of Hg(0) by BrO, at a rate close to that reported by Spicer et al. (*2005*), was necessary to explain the loss of Hg(0). For the Hg(0)+Br oxidation pathway, they had considered the slower reaction rates of Donohoue et al. (*2006*), which are used in this study's 'Std' model, and had included Br and BrO as the second step oxidants. A quick calculation shows that if the oxidation kinetics of the '3xBr' or 'FastK' models are applied after including NO_2 (which was elevated at ~1.5ppbv) as second-step oxidant, the Hg(0)+Br oxidation pathway itself can explain a large fraction of observed depletion rate of Hg(0). Although, the BrO oxidation pathway cannot be entirely ignored, its contribution would be much smaller than what was found by Tas et al. (*2012*) if the '3xBr' and 'FastK' oxidation kinetics are considered.

These MBL studies are consistent with our analysis of the NOMADSS observations in implying much faster oxidation of Hg(0) than currently assumed.

3.7 IMPLICATIONS OF FASTER OXIDATION IN THE GEOS-CHEM MODEL

The annual tropospheric mercury budgets for the three model simulations are presented in Figure 3.7. For all three simulations, the burden of THg and the total emission (and total deposition) fluxes are within 5% of each other (the difference in emissions is from differences in the model-calculated flux of Hg(0) from the oceans). Thus the lifetime of THg is similar for all three simulations ('Std': 8.9 months, '3xBr': 8.4 months, 'FastK': 8.4 months). In order to maintain a similar THg burden for the three simulations, the reduction flux increases two-fold with the '3xBr' simulation and five-fold in the 'FastK' simulation. Both, the '3xBr' and 'FastK' simulations indicate fast cycling between Hg(0) and Hg(II). Considering the global average, in the 'Std' model about 50% of the Hg(II) formed by oxidation deposits to the Earth's surface, whereas in the '3xBr' and 'FastK' simulations, that fraction decreases to 35% and 10% respectively. The higher reduction fluxes in the '3xBr' and the 'FastK' simulations suggest that reduction may also be an important determinant of the distribution of Hg(II) in the atmosphere. This is a significant implication considering the high level of uncertainty in the Hg(II) reduction pathway. This is one more reason why experiments designed to reveal these Hg(II) reduction pathways are critical for a better understanding of the dynamics of mercury in the atmosphere.

The burden of Hg(II) increases by 28% in the ‘3xBr’ simulation relative to the ‘Std’ simulation and by 66% in the ‘FastK’ simulation. As we will see later, most of the global Hg(II) is concentrated in regions where the production (and accumulation) of Hg(II) is efficient, and its global burden increases following an increase in the rate of Hg(II) production. There is a reduction in the lifetime of Hg(0) against oxidation, decreasing from 4.8 months in the ‘Std’ simulation to 2.8 months in the ‘3xBr’ simulation and 1.3 months in the ‘FastK’ simulation. In the ‘3xBr’ simulation, with the higher Br radical concentration between 45°N and 45°S, the Hg(0) lifetime is shorter than the global mean at the lower latitudes, and longer at the high latitudes. Furthermore, the higher in-cloud reduction rate leads to a lower relative contribution of wet deposition compared to dry deposition (including sea-salt uptake) of Hg(II) in the ‘3xBr’ and ‘FastK’ simulations. The shorter Hg(0) lifetimes and changing contributions of wet and dry deposition can lead to different global source-receptor relationships in the ‘3xBr’ and ‘FastK’ simulations compared to the ‘Std’ simulation.

While the atmospheric burden of Hg(II) increases with the ‘3xBr’ and the ‘FastK’ models, the increase is not spatially uniform. Figure 3.8 shows the global distribution and production of Hg(II) at 500 hPa for July 2013. In all three models, enhancements in Hg(II) concentrations are found in the subtropical anticyclones, but the enhancements are higher in the ‘3xBr’ and the ‘FastK’ simulations. For example, in July, the 500 hPa Hg(II) concentration over the eastern US (box 2 in Figure 3.8A-C) is close to 100 pg/m^3 in all three models, but that in the North Pacific anticyclone (box 1 in Figure 3.8A-C) increases from 200 pg/m^3 in the ‘Std’ simulation to 500 pg/m^3 in the ‘FastK’ simulation. The increase in the subtropical Hg(II) concentrations with the ‘3xBr’ and the ‘FastK’ simulations is seen throughout the free troposphere (vertical profile for Box 1 in Figure 3.8D). Over the eastern US (Figure 3.8D), the free tropospheric Hg(II) vertical profiles are similar for the three simulations below 8 km, where the increase in oxidation is matched by the increase in in-cloud reduction. Above 8 km, the absence of liquid clouds prevents reduction from compensating for faster oxidation, which leads to an increase in Hg(II) concentrations in the ‘3xBr’ and ‘FastK’ simulations. Thus, the increase in the global Hg(II) mass burden in the ‘3xBr’ and ‘FastK’ simulations is concentrated largely in the subtropical anticyclones, and, to a smaller extent, in the extra-tropical upper troposphere.

Two processes contribute towards maintaining the high Hg(II) concentrations in these subtropical anticyclones. The anticyclones are characterized by large-scale sinking motion which transports higher Hg(II) concentrations from the upper troposphere to lower altitudes. Hg(II) concentrations are enhanced in the upper troposphere because of faster oxidation of Hg(0) and lack of removal (Figure 3.8H). Oxidation of Hg(0) is faster in upper troposphere because of higher Br radical concentrations, and lower temperatures slowing the thermal dissociation of the HgBr intermediate (Reaction R2, section 2.4.1). Despite lower Hg(II) production rates (Figures 3.8E-G), the 500 hPa Hg(II) concentrations are higher in the southern (winter) hemisphere subtropics compared to the northern hemisphere subtropics. This is likely because the descending branch of the Hadley circulation is stronger in the winter hemisphere, and the downward transport of the upper tropospheric Hg(II) is larger.

Furthermore, the sinking air in the anticyclones suppresses cloud formation and precipitation, in turn, suppressing loss of Hg(II) by in-cloud reduction and wet deposition. This leads to efficient accumulation of Hg(II) in the subtropical anticyclones, even at lower altitudes. At 500hPa, the production of Hg(II) is highest at the north (summer) pole because of the large photolytic source of Br radicals (Figure 3.8E-G), but is compensated by higher loss of Hg(II) from reduction and precipitation, leading to low Hg(II) concentrations. Low 500 hPa Hg(II) concentrations are also seen in regions of the tropics with the largest cloud cover and precipitation (such as the Western Pacific), and in regions with low insolation, such as the southern (winter) hemisphere polar regions.

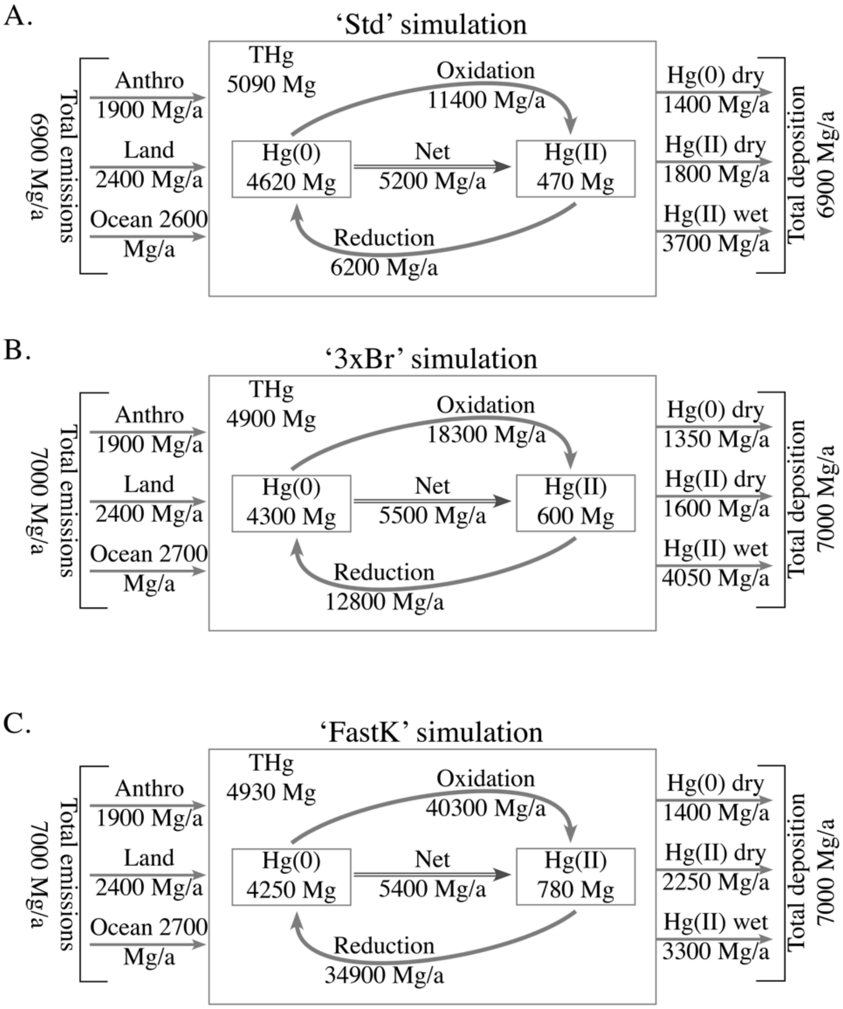

Figure 3.7. Annual (for 2013) global tropospheric budget of mercury in the 'Std' (A), '3xBr' (B), and 'FastK' (C) model simulations. The burdens are in units of Mg (10^6 g) and the fluxes are in units of Mg/a (Mg per year).

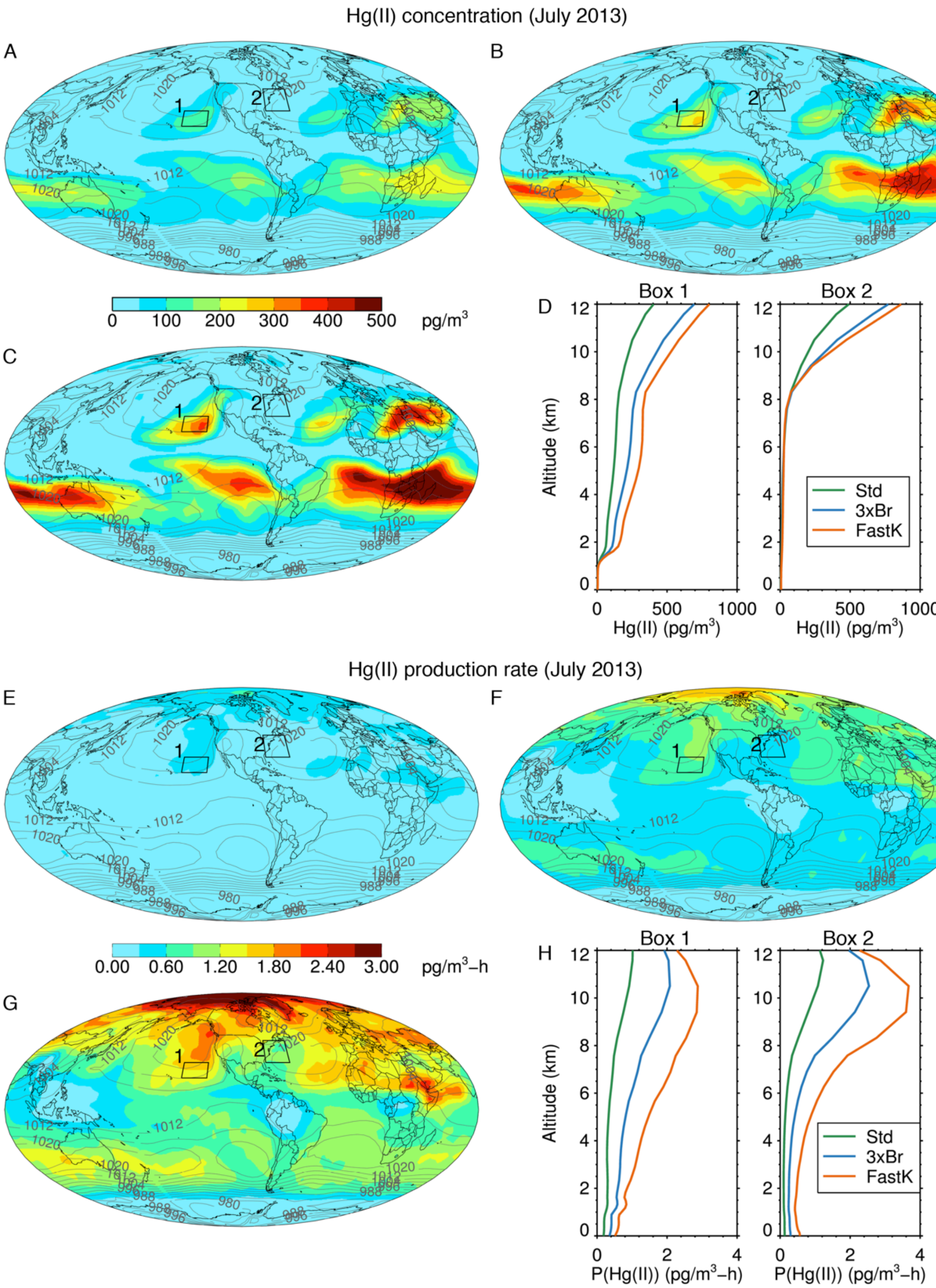

Figure 3.8. Monthly (July 2013) average concentration (A-C) and production rate (E-G) of Hg(II) at 500 hPa, and vertical profiles of the concentration (D) and production rate (H) of Hg(II) for regions marked as ‘1’ and ‘2’ for the ‘Std’, ‘3xBr’ and ‘FastK’ simulations. The contours show the monthly average sea-level pressure (contour interval: 4 hPa).

Chapter 4. CONCLUSIONS AND FUTURE WORK

In this work, I have analyzed the recent aircraft-based measurements of atmospheric mercury species (THg and Hg(II)) made during the NOMADSS experiment which took place over the Southeastern US between June 1 and July 15, 2013.

The mean (± standard deviation) of the observed THg concentrations is 1.49 (±0.16) ng/m^3. The observations show a weak vertical gradient with higher concentrations in the bottom 1 km (1.54 ng/m^3), and lower concentrations between 6 and 7 km (1.42 ng/m^3) in the atmosphere. The near uniform distribution of THg in the lower and middle troposphere is consistent with the ~1 year atmospheric lifetime of THg.

Most of the air samples had Hg(II) concentrations below the instrument limit of detection (LOD). Using the robust Regression on Statistics procedure, the estimated mean Hg(II) concentration for all observations was 111 (± 106) pg/m^3, while the mean of the observations above the LOD was 215 (± 114) pg/m^3. High Hg(II) concentrations, between 300 and 680 pg/m^3, were seen at an altitude of 5-7 km during two flights over Texas and at 1-3 km during one flight over the Atlantic Ocean. These high Hg(II) concentrations were mostly associated with clean subsiding air masses originating in the upper troposphere of the Pacific or Atlantic anticyclones. The low temperatures and high concentrations of the bromine radical in the upper troposphere lead to faster oxidation of Hg(0), while the lack of removal from in-cloud reduction or wet deposition in the anticyclones lead to efficient accumulation of Hg(II).

Results of the GEOS-Chem model were used to interpret these observations. The modeled THg concentrations are in close agreement with the observations, reproducing the horizontal and vertical distribution of THg. The simulated vertical profiles of RH, CO, NO_x, O_3, and CH_2O, too, are in good agreement with the observed vertical profiles. The simulated Hg(II) concentrations, on the other hand, are a factor of 3 lower than the observed concentrations, indicating a faster than expected oxidation of Hg(0) to Hg(II).

I performed two additional simulations with: (i) three times higher Br radical concentrations between 45°N and 45°S and between 750 hPa and the tropopause ('3xBr'), and (ii) higher Hg(0)+Br oxidation rate constant ('FastK'). The model performance improves with both these simulations, especially in air masses with low (< 35%) RH and low (<75 ppbv) CO, where some of the highest Hg(II) concentrations were observed. The model bias decreases from a factor of 3 in the base ('Std') simulation to a factor of 2 in the '3xBr', and a factor of 1.6 in the 'FastK' simulations. The number of data points where the model is within a factor of 2 of the observations increases with '3xBr' (61%) and the 'FastK' (55%) simulations, from that in the 'Std' simulation (24%).

This faster oxidation decreases the lifetime of Hg(0) from 4.8 months in the current simulation to 2.8 months with the '3xBr', and to 1 month with the 'FastK' simulations. To maintain agreement with the global THg burden, the increase in Hg(0) oxidation is balanced by an increase in Hg(II) reduction rates. The contribution of reduction to the loss of Hg(II) increases from 50% in the 'Std' simulation to 65% and 90% in the '3xBr' and the 'FastK' simulations, respectively. In the subtropical anticyclones, the '3xBr' and 'FastK' simulations predict a three- to five-fold enhancement in Hg(II) concentrations at 500 hPa relative to the global average Hg(II) concentration. These subtropical anticyclones are dry, cloud-free regions which provide ideal conditions for accumulation of Hg(II). Future measurements in these regions can help us gain deeper insights into the pathways of Hg(0) oxidation in the atmosphere.

So far, I have compared the results of the '3xBr' and 'FastK' simulations to the NOMADSS observations. Speciated mercury measurements are continuously made at about 30 sites in the AMNet and CAMNet network in North America, and wet deposition measurements are made at about 100 sites in the MDN network. A multi-season comparison of the model results with the speciated measurements at these sites, and with the deposition measurements at the MDN sites is important in further testing the performance of the faster oxidation simulations presented here.

The increase in the importance of Hg(II) reduction with faster Hg(0) oxidation amplifies the effects of the uncertainties in the reduction parameterization. A few different reduction pathways have been proposed based on laboratory experiments. These include reduction in the aqueous phase in the presence of SO_3^- (*van Loon et al., 2000*), carboxylic acids (*Si and Ariya, 2008*), or photolytic reduction even on dry aerosol particles (*Tong et al., 2013*). With better constraints on the oxidation kinetics, these reduction pathways can be evaluated with the GEOS-Chem model. The MDN, AMNet, and CAMNet observations can be used to perform these evaluations.

Although, the NOMADSS observations have provided valuable constraints on the oxidation kinetics of Hg(0), the actual redox chemistry of Hg remains elusive. A focused experiment to measure speciated concentrations of mercury and oxidants (OH, BrO, O_3, HO_2, NO_2) in the subtropical Pacific or Atlantic anticylones, both regions where the model predicts high production and accumulation of Hg(II), would allow to directly test the reaction kinetics of Hg(II) production. The uncertainty of the in-cloud reduction rate of Hg(II) could be decreased by measuring the difference in Hg(II) concentrations upwind and downwind of clouds.

LIST OF ABBREVIATIONS

AMNet	Atmospheric mercury network
CAMNet	Canadian Atmospheric Mercury Network
FAC2	Fraction of points where the model is within a factor of two of the observations or $0.5 \leq M_i/O_i \leq 2$), where O_i is the observation and M_i is the corresponding modeled value
Hg(0)	Gaseous elemental mercury
Hg(II)	Oxidized mercury (gas and particle phase)
HYSPLIT	Hybrid Single Particle Lagrangian Integrated Trajectory Model
LOD	Limit Of Detection
MDN	Mercury Deposition Network
NOMADSS	Nitrogen, Oxidants, Mercury, Aerosols, Distribution. Sources and Sinks
ng/m^3	nanogram per standard cubic meter (1 ng/m^3 of Hg = 0.112 pptv)
NCAR	National Center for Atmospheric Research
NMB	Normalized Mean Bias, NMB $= \sum(M_i - O_i)/\sum O_i \times 100$), where O_i is the observation and M_i is the corresponding modeled value
NSF	National Science Foundation
pg/m^3	picogram per standard cubic meter (1 pg/m^3 = 0.001 ng/m^3)
ppbv	parts per billion by volume (1 ppbv = 10^{-9} mole/mole)
pptv	parts per trillion by volume (1 pptv = 10^{-12} mole/mole)
ROS	Regression on order statistics
STP	Standard Temperature (298.15 K) and Pressure (1 atm)
THg	Total atmospheric mercury (THg = Hg(0) + Hg(II))

BIBLIOGRAPHY

Abbatt, J. P. D., Thomas, J. L., Abrahamsson, K., Boxe, C., Granfors, A., Jones, A. E., Jones, A. E., King, M. D., Saiz-Lopez, A., Shepson, P. B., Sodeau, J., Toohey, D. W., Toubin, C., von Glasow, R., Wren, S. N., & Yang, X. (2012). Halogen activation via interactions with environmental ice and snow in the polar lower troposphere and other regions. *Atmospheric Chemistry and Physics*, *12*(14), 6237-6271.

Ambrose, J. L., Lyman, S. N., Huang, J., Gustin, M. S., & Jaffe, D. A. (2013). Fast time resolution oxidized mercury measurements during the Reno Atmospheric Mercury Intercomparison Experiment (RAMIX). *Environmental science & technology*, *47*(13), 7285-7294.

Ambrose, J.L, Gratz, L.E., Jaffe, D.A., Campos T., Flocke, F.M., Knapp, D.J., Stechman, D.M., Stell, M., Weinheimer, A.J., Cantrell, C.A., & Mauldin III, R.L., (2015). Quantification of mercury emissions from large point sources in the southeastern U.S. during NOMADSS*, Environmental science and technology,* submitted.

Amos, H. M., Jacob, D. J., Holmes, C. D., Fisher, J. A., Wang, Q., Yantosca, R. M., Corbitt, E. S., Galarneau, E., Rutter, A. P., Gustin, M. S., Steffen, A., Schauer, J. J., Graydon, J. A., St. Louis, V. L., Talbot, R. W., Edgerton, E. S., Zhang, Y., & Sunderland, E. M. (2012). Gas-particle partitioning of atmospheric Hg (II) and its effect on global mercury deposition. *Atmospheric Chemistry and Physics*, *12*(1), 591-603.

Amos, H. M., Jacob, D. J., Streets, D. G., & Sunderland, E. M. (2013). Legacy impacts of all-time anthropogenic emissions on the global mercury cycle. *Global Biogeochemical Cycles*, *27*(2), 410-421.

Apel, E. C., Emmons, L. K., Karl, T., Flocke, F., Hills, A. J., Madronich, S., . Lee-Taylor, J., Fried, A., Weibring, P., Walega, J., Richter, D., Tie, X., Mauldin, L., Campos, T., Weinheimer, A., Knapp, D., Sive, B., Kleinman, L., Springston, S., Zaveri, R, Ortega, J., Voss, P., Blake, D., Baker, A., Warneke, C., Welsh-Bon, D., de Gouw, J., Zheng, J., Zhang, R., Rudolph, J., Junkermann, W., & Riemer, D. D. (2010). Chemical evolution of volatile organic compounds in the outflow of the Mexico City Metropolitan area. *Atmos. Chem. Phys*, *10*(5), 2353-2375.

Ariya, P. A., Khalizov, A., & Gidas, A. (2002). Reactions of gaseous mercury with atomic and molecular halogens: kinetics, product studies, and atmospheric implications. *The Journal of Physical Chemistry A*, *106*(32), 7310-7320.

Balabanov, N. B., Shepler, B. C., & Peterson, K. A. (2005). Accurate global potential energy surface and reaction dynamics for the ground state of HgBr2. *The Journal of Physical Chemistry A*, *109*(39), 8765-8773.

Bergan, T., Gallardo, L. A., & Rodhe, H. (1999). Mercury in the global troposphere: a three-dimensional model study. *Atmospheric Environment*, *33*(10), 1575-1585.

Bey, I., Jacob, D. J., Yantosca, R. M., Logan, J. A., Field, B. D., Fiore, A. M., Li, Q., Liu, H. Y., Mickley, L. J., & Schultz, M. G. (2001). Global modeling of tropospheric chemistry with assimilated meteorology: Model description and evaluation. *Journal of Geophysical Research: Atmospheres (1984–2012)*, *106*(D19), 23073-23095.

Bullock, O. R., Atkinson, D., Braverman, T., Civerolo, K., Dastoor, A., Davignon, D., Ku, J-Y, Lohman, K., Myers, T. C., Park, R. J., Seigneur, C., Selin, N.E., Sistla, G., & Vijayaraghavan, K. (2008). The North American Mercury Model Intercomparison Study (NAMMIS): Study description and model‐to‐model comparisons. *Journal of Geophysical Research: Atmospheres (1984–2012)*, *113*(D17).

Bullock, O. R., Atkinson, D., Braverman, T., Civerolo, K., Dastoor, A., Davignon, D. Ku, J-Y, Lohman, K., Myers, T. C., Park, R. J., Seigneur, C., Selin, N.E., Sistla, G., & Vijayaraghavan, K. (2009). An analysis of simulated wet deposition of mercury from the North American Mercury Model Intercomparison Study. *Journal of Geophysical Research: Atmospheres (1984–2012)*, *114*(D8).

Byun, Y., Cho, M., Namkung, W., Lee, K., Koh, D. J., & Shin, D. N. (2010). Insight into the unique oxidation chemistry of elemental mercury by chlorine-containing species: experiment and simulation. *Environmental science & technology*, *44*(5), 1624-1629.

Calvert, J. G., & Lindberg, S. E. (2005). Mechanisms of mercury removal by O_3 and OH in the atmosphere. *Atmospheric Environment*, *39*(18), 3355-3367.

Cobbett, F. D., Steffen, A., Lawson, G., & Van Heyst, B. J. (2007). GEM fluxes and atmospheric mercury concentrations (GEM, RGM and Hgp) in the Canadian Arctic at Alert, Nunavut, Canada (February–June 2005). *Atmospheric Environment*, *41*(31), 6527-6543.

Dastoor, A. P., & Larocque, Y. (2004). Global circulation of atmospheric mercury: a modelling study. *Atmospheric Environment*, *38*(1), 147-161.

Dibble, T. S., Zelie, M. J., & Mao, H. (2012). Thermodynamics of reactions of ClHg and BrHg radicals with atmospherically abundant free radicals. *Atmospheric Chemistry and Physics*, *12*(21), 10271-10279.

Donohoue, D. L., Bauer, D., & Hynes, A. J. (2005). Temperature and pressure dependent rate coefficients for the reaction of Hg with Cl and the reaction of Cl with Cl: A pulsed laser photolysis-pulsed laser induced fluorescence study. *The Journal of Physical Chemistry A*, *109*(34), 7732-7741.

Donohoue, D. L., Bauer, D., Cossairt, B., & Hynes, A. J. (2006). Temperature and pressure dependent rate coefficients for the reaction of Hg with Br and the reaction of Br with Br: A pulsed laser photolysis-pulsed laser induced fluorescence study. *The Journal of Physical Chemistry A*, *110*(21), 6623-6632.

Driscoll, C. T., Mason, R. P., Chan, H. M., Jacob, D. J., & Pirrone, N. (2013). Mercury as a global pollutant: sources, pathways, and effects. *Environmental science & technology*, *47*(10), 4967-4983.

Ebinghaus, R., Kock, H. H., Temme, C., Einax, J. W., Löwe, A. G., Richter, A., Burrows, J.P., & Schroeder, W. H. (2002). Antarctic springtime depletion of atmospheric mercury. *Environmental Science & Technology*, *36*(6), 1238-1244.

Fain, X., Obrist, D., Hallar, A. G., Mccubbin, I., & Rahn, T. (2009). High levels of reactive gaseous mercury observed at a high elevation research laboratory in the Rocky Mountains. *Atmospheric Chemistry and Physics*, *9*(20), 8049-8060.

Fitzgerald, W. F., Lamborg, C. H., & Hammerschmidt, C. R. (2007). Marine biogeochemical cycling of mercury. *Chemical Reviews*, *107*(2), 641-662.

Goodsite, M. E., Plane, J. M. C., & Skov, H. (2004). A theoretical study of the oxidation of Hg0 to HgBr2 in the troposphere. *Environmental science & technology*, *38*(6), 1772-1776.

Goodsite, M. E., Plane, J. M. C., & Skov, H. (2012). Correction to A Theoretical Study of the Oxidation of Hg0 to HgBr2 in the Troposphere. *Environmental science & technology*, *46*(9), 5262-5262.

Gratz, L.E., Shah, V., Ambrose, J.L., Jaffe, D.A., Jaeglé, L., Selin, N.E., Song, S., Festa, J., Stutz, J., Weinheimer, A.J., Knapp, D.J., Montzka, D.D., Campos, T.L., Flocke, F.M., Reeves, M., Stechman, D., Stell, M., Apel, E., Hornbrook, R., Hills, A., Riemer, D., & Blake, N. (2015). Fast oxidation of mercury in the free troposphere. *Nature Geoscience,* submitted.

Gustin, M., & Jaffe, D. (2010). Reducing the uncertainty in measurement and understanding of mercury in the atmosphere. *Environmental science & technology*, *44*(7), 2222-2227.

Gustin, M. S., Huang, J., Miller, M. B., Peterson, C., Jaffe, D. A., Ambrose, J., Finley, B. D., Lyman, S. N., Call, K., Talbot, R., Feddersen, D., Mao, H., & Lindberg, S. E. (2013). Do we understand what the mercury speciation instruments are actually measuring? Results of RAMIX. *Environmental science & technology*, *47*(13), 7295-7306.

Hall, B. (1995). The gas phase oxidation of elemental mercury by ozone. In D. B. Porcella, J. W. Huckabee, & B. Wheatley (Eds.) *Mercury as a Global Pollutant* (pp. 301-315). Springer Netherlands.

Helsel, D. R. (2011). *Statistics for censored environmental data using Minitab and R* (Vol. 77). John Wiley & Sons.

Holmes, C. D., Jacob, D. J., Mason, R. P., & Jaffe, D. A. (2009). Sources and deposition of reactive gaseous mercury in the marine atmosphere. *Atmospheric Environment*, *43*(14), 2278-2285.

Holmes, C. D., Jacob, D. J., Corbitt, E. S., Mao, J., Yang, X., Talbot, R., & Slemr, F. (2010). Global atmospheric model for mercury including oxidation by bromine atoms. *Atmospheric Chemistry and Physics*, *10*(24), 12037-12057.

Hudman, R. C., Jacob, D. J., Turquety, S., Leibensperger, E. M., Murray, L. T., Wu, S., Gilliland, A. B., Avery, M., Bertram, T. H., Brune, W., Cohen, R. C., Dibb, J. E., Flocke, F. M., Fried, A., Holloway, J., Neuman, J. A.,Orville, R.,Perring, A.,Ren, X., Sachse, G. W.,Singh, H. B., Swanson, A.& Wooldridge, P. J. (2007). Surface and lightning sources of nitrogen oxides over the United States: Magnitudes, chemical evolution, and outflow. *Journal of Geophysical Research: Atmospheres (1984–2012), 112*(D12).

Hynes, A. J., Donohoue, D. L., Goodsite, M. E., & Hedgecock, I. M. (2009). Our current understanding of major chemical and physical processes affecting mercury dynamics in the atmosphere and at the air-water/terrestrial interfaces. In N.Pirrone, & R. Mason (Eds.), *Mercury fate and transport in the global atmosphere* (pp. 427-457). Springer US.

Jaeglé, L., Strode, S., Selin, N. E., & Jacob, D.J. (2009), The GEOS-Chem Model, In N.Pirrone, & R. Mason (Eds.), *Mercury Fate and Transport in the Global Atmosphere* (pp. 533-545), Springer US.

Jaffe, D. A., Lyman, S., Amos, H. M., Gustin, M. S., Huang, J., Selin, N. E., Levin, L., ter Schure, A., Mason, R. P., Talbot, R., Rutter, A.P., Finley, B., Jaeglé,, L., Shah, V., McClure, C., Ambrose, J., Gratz, L., Lindberg, S., Weiss-Penzias, P., Sheu, G.-R., Feddersen, D., Horvat., M., Dastoor, A., Hynes, A., Mao, H., Sonke, J.E., Slemr, F., Fisher, J.A., Ebinghaus, R., Zhang, Y., & Edwards, G. (2014). Progress on understanding atmospheric mercury hampered by uncertain measurements. *Environmental science & technology*, *48*(13), 7204-7206.

Jung, G., Hedgecock, I.M.,& Pirrone, N. (2009), The ECHMERT Model, In N.Pirrone, & R. Mason (Eds.), *Mercury Fate and Transport in the Global Atmosphere* (pp. 547-569), Springer US.

Karagas, M., Choi, A. L., Oken, E., Horvat, M., Schoeny, R., Kamai, E., Grandjean, P., & Korrick, S. (2012). Evidence on the human health effects of low level methylmercury exposure. *Environmental health perspectives*, *120*(6), 799-806.

Khalizov, A. F., Viswanathan, B., Larregaray, P., & Ariya, P. A. (2003). A theoretical study on the reactions of Hg with halogens: Atmospheric implications. *The Journal of Physical Chemistry A*, *107*(33), 6360-6365.

Kos, G., Ryzhkov, A., Dastoor, A., Narayan, J., Steffen, A., Ariya, P. A., & Zhang, L. (2013). Evaluation of discrepancy between measured and modelled oxidized mercury species. *Atmospheric Chemistry and Physics*, *13*(9), 4839-4863.

Lamborg, C. H., Fitzgerald, W. F., O'Donnell, J., & Torgersen, T. (2002). A non-steady-state compartmental model of global-scale mercury biogeochemistry with interhemispheric atmospheric gradients. *Geochimica et Cosmochimica Acta*, *66*(7), 1105-1118.

Landis, M. S., Lynam, M. M., & Stevens, R. K. (2005). The monitoring and modelling of Hg species in support of local, regional and global modelling. In N. Pirrone & K.R. Mahaffey (Eds.), *Dynamics of Mercury Pollution on Regional and Global Scales:* (pp. 123-151). Springer US.

Laurier, F. J., Mason, R. P., Whalin, L., & Kato, S. (2003). Reactive gaseous mercury formation in the North Pacific Ocean's marine boundary layer: A potential role of halogen chemistry. *Journal of Geophysical Research: Atmospheres (1984–2012)*, *108*(D17).

Li, P., Feng, X., & Qiu, G. (2010). Methylmercury exposure and health effects from rice and fish consumption: a review. *International journal of environmental research and public health*, *7*(6), 2666-2691.

Lin, S. J., & Rood, R. B. (1996). Multidimensional flux-form semi-Lagrangian transport schemes. *Monthly Weather Review*, *124*(9), 2046-2070.

Lin, J.-T., & McElroy, M. B. (2010). Impacts of boundary layer mixing on pollutant vertical profiles in the lower troposphere: Implications to satellite remote sensing. *Atmospheric Environment*, *44*(14), 1726-1739.

Lindberg, S. E., Brooks, S., Lin, C. J., Scott, K. J., Landis, M. S., Stevens, R. K., Goodsite, M.E., & Richter, A. (2002). Dynamic oxidation of gaseous mercury in the Arctic troposphere at polar sunrise. *Environmental Science & Technology*, *36*(6), 1245-1256.

Lindberg, S., Bullock, R., Ebinghaus, R., Engstrom, D., Feng, X., Fitzgerald, W., Pirrone, N., Prestbo, E., & Seigneur, C. (2007). A synthesis of progress and uncertainties in attributing the sources of mercury in deposition. *AMBIO: A Journal of the Human Environment*, *36*(1), 19-33.

Liu, H., Jacob, D. J., Bey, I., & Yantosca, R. M. (2001). Constraints from 210Pb and 7Be on wet deposition and transport in a global three-dimensional chemical. *Journal of Geophysical Research*, *106*(D11), 12-109.

Lyman, S. N., Jaffe, D. A., & Gustin, M. S. (2010). Release of mercury halides from KCl denuders in the presence of ozone. *Atmospheric Chemistry and Physics*, *10*(17), 8197-8204.

Lyman, S. N., & Jaffe, D. A. (2012). Formation and fate of oxidized mercury in the upper troposphere and lower stratosphere. *Nature Geoscience*, *5*(2), 114-117.

Mao, H., Talbot, R. W., Sive, B. C., Kim, S. Y., Blake, D. R., & Weinheimer, A. J. (2010). Arctic mercury depletion and its quantitative link with halogens. *Journal of atmospheric chemistry*, *65*(2-3), 145-170.

Mason, R. P., & Sheu, G. R. (2002). Role of the ocean in the global mercury cycle. *Global biogeochemical cycles*, *16*(4), 40-1.

McClure, C. D., Jaffe, D. A., & Edgerton, E. S. (2014). Evaluation of the KCl Denuder Method for Gaseous Oxidized Mercury using HgBr2 at an In-Service AMNet Site. *Environmental science & technology*, *48*(19), 11437-11444.

Mergler, D., Anderson, H. A., Chan, L. H. M., Mahaffey, K. R., Murray, M., Sakamoto, M., & Stern, A. H. (2007). Methylmercury exposure and health effects in humans: a worldwide concern. *AMBIO: A Journal of the Human Environment*, *36*(1), 3-11.

Morel, F. M., Kraepiel, A. M., & Amyot, M. (1998). The chemical cycle and bioaccumulation of mercury. *Annual review of ecology and systematics*, 543-566.

Neuman, J. A., Trainer, M., Aikin, K. C., Angevine, W. M., Brioude, J., Brown, S. S., de Gouw, J. A., Dube, W. P., Flynn, J. H., Graus, M., Holloway, J. S., Lefer, B. L., Nedelec, P., Nowak, J. B, Parrish, D. D., Pollack, I. B, Roberts, J. M., Ryerson, T. B., Smit, H, Thouret, V., & Wagner, N. L. (2012). Observations of ozone transport from the free troposphere to the Los Angeles basin. *Journal of Geophysical Research: Atmospheres (1984–2012)*, *117*(D21).

Obrist, D., Tas, E., Peleg, M., Matveev, V., Faïn, X., Asaf, D., & Luria, M. (2011). Bromine-induced oxidation of mercury in the mid-latitude atmosphere. *Nature Geoscience*, *4*(1), 22-26.

Pacyna, E. G., Pacyna, J. M., Sundseth, K., Munthe, J., Kindbom, K., Wilson, S., Steenhuisen, F., & Maxson, P. (2010). Global emission of mercury to the atmosphere from anthropogenic sources in 2005 and projections to 2020. *Atmospheric Environment*, *44*(20), 2487-2499.

Pal, B., & Ariya, P. A. (2004a). Studies of ozone initiated reactions of gaseous mercury: kinetics, product studies, and atmospheric implications. *Physical Chemistry Chemical Physics*, *6*(3), 572-579.

Pal, B., & Ariya, P. A. (2004b). Gas-phase HO-initiated reactions of elemental mercury: kinetics, product studies, and atmospheric implications. *Environmental science & technology*, *38*(21), 5555-5566.

Parrella, J. P., Jacob, D. J., Liang, Q., Zhang, Y., Mickley, L. J., Miller, B., Evans, M. J., Yang, X., Pyle, J. A., Theys, N., & Roozendael, M. V. (2012). Tropospheric bromine chemistry:

implications for present and pre-industrial ozone and mercury. *Atmospheric Chemistry and Physics*, *12*(15), 6723-6740.

Pirrone, N., Cinnirella, S., Feng, X., Finkelman, R. B., Friedli, H. R., Leaner, J., Mason, R., Mukherjee, A. B., Stracher, G. B., Streets, D. G., & Telmer, K. (2010). Global mercury emissions to the atmosphere from anthropogenic and natural sources. *Atmospheric Chemistry and Physics*, *10*(13), 5951-5964.

Platt, U., & Stutz, J. (2008). Measurement Techniques for Atmospheric Trace Gas Concentrations and Other Parameters. In *Differential Optical Absorption Spectroscopy* (pp. 113-134). Springer Berlin Heidelberg.

Poissant, L., Pilote, M., Beauvais, C., Constant, P., & Zhang, H. H. (2005). A year of continuous measurements of three atmospheric mercury species (GEM, RGM and Hg_p) in southern Québec, Canada. *Atmospheric Environment*, *39*(7), 1275-1287.

Raofie, F., & Ariya, P. A. (2004). Product study of the gas-phase BrO-initiated oxidation of Hg0: evidence for stable Hg1+ compounds. *Environmental science & technology*, *38*(16), 4319-4326.

Raofie, F., Snider, G., & Ariya, P. A. (2008). Reaction of gaseous mercury with molecular iodine, atomic iodine, and iodine oxide radicals-Kinetics, product studies, and atmospheric implications. *Canadian Journal of Chemistry*, *86*(8), 811-820.

Reinecker, M. M., Suarez, M. J., Todling, R., Bacmeister, J., Takacs, L., Liu, H. C., Gu., W., Sienkiewicz, M., Koster, R. D., Gelaro, R., Stajner, I., & Nielsen, J. E. (2008). The GEOS-5 Data Assimilation System-Documentation of Versions 5.0. 1, 5.1. 0. *NASA Tech Rep. TM-2007*, *104606*

Ridley, B., Atlas, E., Selkirk, H., Pfister, L., Montzka, D., Walega, J., Donnelly, S., Stroud, V., Richard, E., Kelly, K., Tuck, A., Thompson, T., Reeves, J., Baumgardner, D., Rawlins, W.T., Mahoney, M., Herman, R., Friedl, R., Moore, F., Ray, E, & Elkins, J. (2004). Convective transport of reactive constituents to the tropical and mid-latitude tropopause region: I. Observations. *Atmospheric Environment*, *38*(9), 1259-1274.

Rutter, A. P., Shakya, K. M., Lehr, R., Schauer, J. J., & Griffin, R. J. (2012). Oxidation of gaseous elemental mercury in the presence of secondary organic aerosols. *Atmospheric Environment*, *59*, 86-92.

Scheuhammer, A. M., Meyer, M. W., Sandheinrich, M. B., & Murray, M. W. (2007). Effects of environmental methylmercury on the health of wild birds, mammals, and fish. *AMBIO: A Journal of the Human Environment*, *36*(1), 12-19.

Selin, N. E., & Jacob, D. J. (2008). Seasonal and spatial patterns of mercury wet deposition in the United States: Constraints on the contribution from North American anthropogenic sources. *Atmospheric Environment*, *42*(21), 5193-5204.

Selin, N. E., Jacob, D. J., Yantosca, R. M., Strode, S., Jaegle, L., & Sunderland, E. M. (2008). Global 3‐D land‐ocean‐atmosphere model for mercury: Present‐day versus preindustrial cycles and anthropogenic enrichment factors for deposition. *Global Biogeochemical Cycles*, *22*(2).

Selin, N. E. (2009). Global biogeochemical cycling of mercury: a review. *Annual Review of Environment and Resources*, *34*(1), 43.

Seigneur, C., Karamchandani, P., Lohman, K., Vijayaraghavan, K., & Shia, R. L. (2001). Multiscale modeling of the atmospheric fate and transport of mercury. *Journal of Geophysical Research: Atmospheres (1984–2012)*, *106*(D21), 27795-27809.

Shepler, B. C., Balabanov, N. B., & Peterson, K. A. (2007). Hg+ Br→ HgBr recombination and collision-induced dissociation dynamics. *The Journal of chemical physics*, *127*(16), 164304.

Sheu, G. R., Lin, N. H., Wang, J. L., Lee, C. T., Ou Yang, C. F., & Wang, S. H. (2010). Temporal distribution and potential sources of atmospheric mercury measured at a high-elevation background station in Taiwan. *Atmospheric Environment*, *44*(20), 2393-2400.

Si, L., & Ariya, P. A. (2008). Reduction of Oxidized Mercury Species by Dicarboxylic Acids (C2− C4): Kinetic and Product Studies. *Environmental science & technology*, *42*(14), 5150-5155.

Sillman, S., Marsik, F. J., Al‐Wali, K. I., Keeler, G. J., & Landis, M. S. (2007). Reactive mercury in the troposphere: Model formation and results for Florida, the northeastern United States, and the Atlantic Ocean. *Journal of Geophysical Research: Atmospheres (1984–2012)*, *112*(D23).

Soerensen, A. L., Sunderland, E. M., Holmes, C. D., Jacob, D. J., Yantosca, R. M., Skov, H., Christensen, J. H., Strode, S. A., & Mason, R. P. (2010). An improved global model for air-sea exchange of mercury: High concentrations over the North Atlantic. *Environmental science & technology*, *44*(22), 8574-8580.

Sommar, J., Hallquist, M., Ljungström, E., & Lindqvist, O. (1997). On the gas phase reactions between volatile biogenic mercury species and the nitrate radical. *Journal of Atmospheric Chemistry*, *27*(3), 233-247.

Sommar, J., Gårdfeldt, K., Strömberg, D., & Feng, X. (2001). A kinetic study of the gas-phase reaction between the hydroxyl radical and atomic mercury. *Atmospheric Environment*, *35*(17), 3049-3054.

Song, S., Selin, N.E., Giang, Jaffe., D.A., Jaeglé, L., Gratz, L.E., Ambrose, J.L., Shah, V., & Giang, A. (2015). GEOS-Chem simulation for NOMADSS Hg measurements: Comparison between over-land and over-ocean flights. Manuscript in preparation.

Spicer, C. W., Satola, J., Abbgy, A. A., Plastridge, R. A., & Cowen, K. A. (2002). Kinetics of Gas-Phase Elemental Mercury Reactions with Halogen Species, Ozone, and Nitrate Radical under Atmospheric Conditions. *FL, Florida Department of Environmental Protection*, 1-20.

Sprovieri, F., Hedgecock, I. M., & Pirrone, N. (2010a). An investigation of the origins of reactive gaseous mercury in the Mediterranean marine boundary layer. *Atmospheric Chemistry and Physics*, *10*(8), 3985-3997.

Sprovieri, F., Pirrone, N., Ebinghaus, R., Kock, H., & Dommergue, A. (2010b). A review of worldwide atmospheric mercury measurements. *Atmospheric Chemistry and Physics*, *10*(17), 8245-8265.

Strode, S. A., Jaeglé, L., Selin, N. E., Jacob, D. J., Park, R. J., Yantosca, R. M., Mason, R. P., & Slemr, F. (2007). Air-sea exchange in the global mercury cycle. *Global Biogeochemical Cycles*, *21*(1).

Subir, M., Ariya, P. A., & Dastoor, A. P. (2011). A review of uncertainties in atmospheric modeling of mercury chemistry I. Uncertainties in existing kinetic parameters–Fundamental limitations and the importance of heterogeneous chemistry. *Atmospheric Environment*, *45*(32), 5664-5676.

Sumner, A. L., Spicer, C. W., Satola, J., Mangaraj, R., Cowen, K. A., Landis, M. S., Stevens, R. K., & Atkeson, T. D. (2005). Environmental chamber studies of mercury reactions in the atmosphere. In N. Pirrone & K.R. Mahaffey (Eds.), *Dynamics of Mercury Pollution on Regional and Global Scales:* (pp. 193-212). Springer US.

Swartzendruber, P. C., Jaffe, D. A., Prestbo, E. M., Weiss-Penzias, P., Selin, N. E., Park, R., Jacob, D. J., Strode, S., & Jaegle, L. (2006). Observations of reactive gaseous mercury in the free troposphere at the Mount Bachelor Observatory. *Journal of Geophysical Research: Atmospheres (1984–2012)*, *111*(D24).

Swartzendruber, P. C., Jaffe, D. A., & Finley, B. (2009). Development and first results of an aircraft-based, high time resolution technique for gaseous elemental and reactive (oxidized) gaseous mercury. *Environmental science & technology*, *43*(19), 7484-7489.

Talbot, R., Mao, H., Scheuer, E., Dibb, J., & Avery, M. (2007). Total depletion of Hg in the upper troposphere–lower stratosphere. *Geophysical Research Letters*, *34*(23).

Tas, E., Obrist, D., Peleg, M., Matveev, V., Faïn, X., Asaf, D., & Luria, M. (2012). Measurement-based modelling of bromine-induced oxidation of mercury above the Dead Sea. *Atmospheric Chemistry and Physics*, *12*(5), 2429-2440.

Theys, N., Roozendael, M. V., Hendrick, F., Yang, X., Smedt, I. D., Richter, A., Begoin, M., Errera, Q., Johnston, P. V., Kreher, K. & Mazière, M. D. (2011). Global observations of tropospheric BrO columns using GOME-2 satellite data. *Atmospheric Chemistry and Physics*, *11*(4), 1791-1811.

Tong, Y., Eichhorst, T., Olson, M. R., McGinnis, J. E., Turner, I., Rutter, A. P., Shafer, M. M., Wang, X., & Schauer, J. J. (2013). Atmospheric photolytic reduction of Hg (II) in dry aerosols. *Environmental Science: Processes & Impacts*, *15*(10), 1883-1888.

Tossell, J. A. (2006). Calculation of the energetics for the oligomerization of gas phase HgO and HgS and for the solvolysis of crystalline HgO and HgS. *The Journal of Physical Chemistry A*, *110*(7), 2571-2578.

Travnikov O., Lin C.-J. Dastoor A., Bullock O.R., Hedgecock I.M., Holmes C., Ilyin I., Jaegle L., Jung G., Pan L., Pongprueksa P., Ryzhkov A., Seigneur C., & Skov H. (2010) Global and regional modeling. In N. Pirrone & T. Keating (Eds.) *HTAP 2010 Assessment Report. Part B, Mercury:* (pp. 97-144). Geneva: UN-Economic Comision for Europe.

van Loon, L., Mader, E., & Scott, S. L. (2000). Reduction of the aqueous mercuric ion by sulfite: UV spectrum of HgSO3 and its intramolecular redox reaction. *The Journal of Physical Chemistry A*, *104*(8), 1621-1626.

von Glasow, R., Kuhlmann, R. V., Lawrence, M. G., Platt, U., & Crutzen, P. J. (2004). Impact of reactive bromine chemistry in the troposphere. *Atmospheric Chemistry and Physics*, *4*(11/12), 2481-2497.

Wang, Y., Logan, J. A., & Jacob, D. J. (1998). Global simulation of tropospheric O3-NO x-hydrocarbon chemistry: 2. Model evaluation and global ozone budget. *Journal of Geophysical Research: Atmospheres (1984–2012)*, *103*(D9), 10727-10755.

Wang, Q., Jacob, D. J., Fisher, J. A., Mao, J., Leibensperger, E. M., Carouge, C. C., Le Sager, P., Kondo, Y., Jimenez, J. L., Cubison, M. J., & Doherty, S. J. (2011). Sources of carbonaceous aerosols and deposited black carbon in the Arctic in winter-spring: implications for radiative forcing. *Atmospheric Chemistry and Physics*, *11*(23), 12453-12473.

Wang, F., Saiz-Lopez, A., Mahajan, A. S., Gómez Martín, J. C., Armstrong, D., Lemes, M., Hay, T., & Prados-Roman, C. (2014). Enhanced production of oxidised mercury over the tropical Pacific Ocean: a key missing oxidation pathway. *Atmospheric Chemistry and Physics*, *14*(3), 1323-1335.

Weiss-Penzias, P., Amos, H. M., Selin, N. E., Sexauer Gustin, M., Jaffe, D. A., Obrist, D., Sheu, G.R., & Giang, A. (2015). Use of a global model to understand speciated atmospheric mercury observations at five high-elevation sites. *Atmospheric Chemistry and Physics*, *15*, 1161-1173.

Wu, S., Mickley, L. J., Jacob, D. J., Logan, J. A., Yantosca, R. M., & Rind, D. (2007). Why are there large differences between models in global budgets of tropospheric ozone?. *Journal of Geophysical Research: Atmospheres (1984–2012)*, *112*(D5).

Yang, X., Cox, R. A., Warwick, N. J., Pyle, J. A., Carver, G. D., O'Connor, F. M., & Savage, N. H. (2005). Tropospheric bromine chemistry and its impacts on ozone: A model study. *Journal of Geophysical Research: Atmospheres (1984–2012)*, *110*(D23).

Zhang, L., Jacob, D. J., Downey, N. V., Wood, D. A., Blewitt, D., Carouge, C. C., van Donkelaar, A., Jones, D., Murray, L. T., & Wang, Y. (2011). Improved estimate of the policy-relevant background ozone in the United States using the GEOS-Chem global model with 1/2×2/3 horizontal resolution over North America. *Atmospheric Environment*, *45*(37), 6769-6776.

Zhang, Y., Jaeglé, L., Donkelaar, A. V., Martin, R. V., Holmes, C. D., Amos, H. M., Wang, Q., Talbot, R., Artz, R., Brooks, S., Luke, W., Holsen, T. M., Felton, D., Miller, E. K., Perry, K. D., Schmeltz, D., Steffen, A., Tordon, R., Weiss-Penzias, P., & Zsolway, R. (2012). Nested-grid simulation of mercury over North America. *Atmospheric Chemistry and Physics*, *12*(14), 6095-6111.

Zhang, Y., Jaeglé, L., Thompson, L., & Streets, D. G. (2014). Six centuries of changing oceanic mercury. *Global Biogeochemical Cycles*, *28*(11), 1251-1261